

Simulating linear optical properties of molecules on a superconducting quantum processor

Kaixuan Huang^{2,3†}, Xiaoxia Cai^{1†}, Hao Li^{3,7†}, Zi-Yong Ge⁵, Ruijuan Hou¹, Hekang Li³, Tong Liu^{3,4}, Yunhao Shi^{3,4}, Chitong Chen^{3,4}, Dongning Zheng^{3,4,6}, Kai Xu^{3,4,6*}, Zhi-Bo Liu^{2*}, Zhendong Li^{1*}, Heng Fan^{3,4,6*}, Wei-Hai Fang¹

¹ Key Laboratory of Theoretical and Computational Photochemistry, Ministry of Education, College of Chemistry, Beijing Normal University, Beijing 100875, China

² The Key Laboratory of Weak Light Nonlinear Photonics, Ministry of Education, Teda Applied Physics Institute and School of Physics, Nankai University, Tianjin 300457, China

³ Institute of Physics, Chinese Academy of Sciences, Beijing 100190, China

⁴ School of Physical Sciences, University of Chinese Academy of Sciences, Beijing 100190, China

⁵ Theoretical Quantum Physics Laboratory, RIKEN Cluster for Pioneering Research, Wako-shi, Saitama 351-0198, Japan

⁶ CAS Center for Excellence in Topological Quantum Computation, University of Chinese Academy of Sciences, Beijing 100190, China

⁷ School of Physics, Northwest University, Xi'an 710127, China

[†] These authors contributed equally;

* To whom correspondence should be addressed;

E-mail: kaixu@iphy.ac.cn, liuzb@nankai.edu.cn, zhendongli@bnu.edu.cn, hfan@iphy.ac.cn

Predictive simulation of molecular response properties such as electronic absorption spectra is of great technological importance, but remains a long-standing computational challenge for electronic structure methods on classical computers. While quantum computers hold the promise to solve this

problem more efficiently in the long run, existing quantum algorithms requiring deep quantum circuits are infeasible for near-term noisy quantum processors. Here, we report the first ever simulation of linear optical properties of molecules on a superconducting quantum processor enabled by a hybrid quantum-classical approach. We demonstrate the feasibility of this approach for computing dynamic polarizabilities of the hydrogen molecule, and then apply it to tackle two representative problems of practical significance, including simulating ultraviolet-visible absorption spectra of polyacenes and X-ray absorption spectra of carbon monoxide. These results represent an initial step towards exploring quantum computing for reliably simulating linear and nonlinear response properties of more challenging systems in the near future.

In silico simulation of molecular response properties, such as dynamic polarizabilities, absorption/emission spectra, and nonlinear optical properties, has become an essential component in virtual design of new materials with specific properties [1]. The need for accurate and efficient computational tools is more urgent than before in the era of data driven material research, since they can significantly accelerate the high-throughput screening of the enormous candidates. Despite decades of effort and tremendous progress in methodological developments, predictive simulation of molecular response properties remains a fundamental challenge for electronic structure methods on classical computers [1, 2]. While density functional theory (DFT) and its time-dependent extension (TD-DFT) have been the workhorse for simulating structural and response properties of large molecules, the limitations of density functional approximations are well-known [4], especially for strongly correlated systems. More accurate wavefunction-based methods are constrained to small molecules by their steep computational scaling with respect to the system size [2]. In particular, the exact method for solving the many-electron Schrödinger equation within a given basis set, full configuration interaction (FCI) or

exact diagonalization, has an exponential scaling in both physical memory and computational time.

A promising way to overcome the *exponential wall* in simulating interacting many-body systems is to use quantum computers, which are controllable quantum mechanical devices as initially suggested by Feynman [5]. Recent breakthroughs in quantum computing technology with superconducting quantum processors have achieved the quantum computational advantage for specific sampling problems [6, 7], for which quantum computers can outperform the most powerful current supercomputers. Identifying a similar advantage by designing efficient algorithms for solving nontrivial practical problems on these noisy intermediate-scale quantum [8] (NISQ) devices will be the next milestone. Quantum chemistry is one of the most promising fields [9–11], where NISQ devices may offer a practical quantum advantage for useful problems such as designing new catalysts for nitrogen fixation [12, 13]. Previous quantum simulations of molecules have almost exclusively focused on solving the ground-state problem [6, 7, 14–16], which is the very first step towards simulating molecular properties. The variational quantum eigensolver [6, 7] (VQE), belonging to the class of hybrid quantum-classical algorithms [19], has attracted much interest due to its feasibility on NISQ devices. In VQE, the requirement of long coherent operations in traditional quantum algorithms such as quantum phase estimation (QPE) [14–16, 20] is traded by many measurements of shallow parameterized quantum circuits (PQCs) for computing the energy expectation value and classical optimization for updating variational parameters. It has been experimentally demonstrated for prototypical molecules, e.g., H_2 [6, 21–24], LiH [22, 23, 25], BeH_2 [22], and hydrogen chains [26]. Due to the inherent noises [23] in NISQ devices, errors in the computed ground-state energies are relatively high (ca. 0.1 Hartree [26]) and grow rapidly with the increase of the molecular size and the depth of PQCs. Thus, various error mitigation (EM) techniques [10] have been developed to improve the VQE energy in order to reach the chemical accuracy (ca. 1 milli-Hartree).

After preparing the ground state on quantum computers, molecular properties described by ground-state expectation values, such as dipole moments [25], can be trivially computed by measurements. In contrast, computing linear and nonlinear response properties is far more challenging, because they implicitly involve not only the ground state but also all the excited states [1]. Existing quantum algorithms for linear response functions largely rely on computing time-correlation functions using quantum computers [14, 29, 30], which can later be Fourier transformed to the frequency domain. We have recently proposed a different quantum algorithm for computing response properties in the frequency domain [8], by using quantum algorithms such as the Harrow-Hassidim-Lloyd algorithm [32] as subroutines for solving linear response equations on quantum computers. Theoretically, all these quantum algorithms promise an exponential speedup over classical FCI-based response algorithms [2]. Unfortunately, they are generally infeasible for molecules on NISQ devices, due to the requirement of deep quantum circuits for implementing the time evolution $e^{-i\hat{H}_0 t}$ with the molecular Hamiltonian \hat{H}_0 [16] as a common component in these algorithms. Therefore, how to compute response properties of molecules by leveraging the power of NISQ devices remains a highly nontrivial open problem and has not been experimentally demonstrated.

Here, we describe a pragmatic hybrid quantum-classical approach more suitable for NISQ devices, termed the variational quantum response (VQR) approach. We implement it on a state-of-the-art superconducting quantum processor with all-to-all qubit connectivity [16, 34] to realize the first ever quantum simulation of linear optical properties of molecules. The feasibility of VQR is benchmarked for computing dynamic polarizabilities of the hydrogen molecule (H_2) at three geometries with different electron correlation strengths. We then apply it to tackle two representative problems of practical significance, viz., simulating ultraviolet-visible (UV-Vis) absorption spectra of polyacenes and X-ray absorption spectra of carbon monoxide (CO). These results pave the way for exploring the power of quantum computing for simulating re-

sponse properties of more complicated systems in future.

Results

Variational quantum response (VQR) approach

We outline how VQR works for simulating linear response properties, which characterize the first order response of molecules to an applied external field and are essential for understanding absorption and emission properties of materials. Further details are provided in the Methods section and Supplementary Section 1. Specifically, we consider the following linear response function

$$\chi(\omega) = \sum_k \frac{|\langle \Psi_k | \hat{V} | \Psi_0 \rangle|^2}{\omega_{k0} - (\omega + i\gamma)}, \quad (1)$$

where ω is the frequency of the external field and γ is a broadening parameter. This function encodes all the information of the excitation process from the ground state $|\Psi_0\rangle$ to the k -th excited state $|\Psi_k\rangle$ due to the perturbation \hat{V} , i.e., the excitation energy $\omega_{k0} = E_k - E_0$ and the corresponding transition amplitude $|\langle \Psi_k | \hat{V} | \Psi_0 \rangle|^2$. Here, we focus on the case where \hat{V} is a dipole operator $\{\hat{x}, \hat{y}, \hat{z}\}$, such that $\chi(\omega)$ represents the resonant contribution to dipole polarizability, whose imaginary part is related with the linear absorption of radiation $\sigma_{\text{abs}}(\omega)$ by a randomly oriented molecular sample in the electric-dipole approximation [1], viz., $\sigma_{\text{abs}}(\omega) = \frac{4\pi\omega}{c} \text{Im}\bar{\chi}(\omega)$ with $\bar{\chi} = \frac{1}{3}(\chi_{xx} + \chi_{yy} + \chi_{zz})$ and c being the speed of light.

Exact calculations of $\chi(\omega)$ are intractable on classical computers, as the number of excited states scales exponentially with the system size. To compute $\chi(\omega)$ with quantum processors, the first step is to map the problem of interacting electrons to a corresponding problem of qubits, each of which is a two-level quantum system and forms the fundamental unit of quantum computers. As shown in Fig. 1a, this preprocessing step starts with a classical quantum chemical calculation of molecules, typically using self-consistent field methods, to obtain a

set of molecular orbitals (MOs). Then, a fermion-to-qubit mapping [4, 5] is chosen to transform the second-quantized \hat{H}_0 and \hat{V} for electrons to their counterparts for n qubits, which are linear combinations of Pauli terms, e.g., $\hat{H}_0 = \sum_k h_k P_k$ with $P_k = \sigma_0^k \otimes \sigma_1^k \otimes \cdots \otimes \sigma_{n-1}^k$ being a tensor product of Pauli operators ($\sigma_i \in \{I, X, Y, Z\}$). The next step is to prepare the ground state $|\Psi_0\rangle$ using VQE [6, 7] (see Fig. 1b). As exemplified in Fig. 1b, a PQC $U_0(\vec{\theta}_0)$ composed of parameterized single-qubit and two-qubit quantum gates (e.g., Z_θ and $\sqrt{i\text{SWAP}}$) with a set of free angles $\vec{\theta}_0$ is designed to evolve the initial state $|0\rangle$ to a target state, i.e., $|\Psi_0\rangle = U_0(\vec{\theta}_0)|0\rangle$. The optimal parameters $\vec{\theta}_0^{\text{opt}}$ are determined by classically minimizing the energy function $E(\vec{\theta}_0) = \langle\Psi_0|\hat{H}|\Psi_0\rangle = \sum_k h_k \langle\Psi_0|P_k|\Psi_0\rangle$, with the necessary expectation values $\langle\Psi_0|P_k|\Psi_0\rangle$ measured on quantum processors.

Given the ground state, we propose a two-step VQR approach in conjunction with a symmetry-based EM strategy for computing $\chi(\omega)$ in an interested frequency region (see Fig. 1c). To circumvent the prohibitive sum over excited states in Eq. (23), an auxiliary response state $|\Psi(\omega)\rangle$ is defined by a linear response equation [8]

$$\hat{A}(\omega)|\Psi(\omega)\rangle = \hat{V}|\Psi_0\rangle, \quad \hat{A}(\omega) = \hat{H}_0 - E_0 - (\omega + i\gamma), \quad (2)$$

such that $\chi(\omega)$ becomes a simple expectation value $\chi(\omega) = \langle\Psi(\omega)|\hat{A}^\dagger(\omega)|\Psi(\omega)\rangle$, similar to the energy. On classical computers, both solving the linear system of equations (2) and computing the expectation value for $\chi(\omega)$ scale exponentially in n . Following the variational hybrid quantum-classical algorithm [9, 10] for linear system of equations, we present a pragmatic algorithmic primitive for solving the linear response equation on NISQ devices, which can also be extended to high-order response equations for nonlinear response properties. Specifically, we introduce a PQC for the normalized response state $|x\rangle = |\Psi(\omega)\rangle/\| |\Psi(\omega)\rangle \| = U_1(\vec{\theta}_1)|0\rangle$, and find the optimal parameters $\vec{\theta}_1^{\text{opt}}$ by minimizing a cost function

$$L(\vec{\theta}_1) = \langle\Psi_0|\hat{V}^\dagger\hat{V}|\Psi_0\rangle\langle x|\hat{A}^\dagger(\omega)\hat{A}(\omega)|x\rangle - |\langle\Psi_0|\hat{V}^\dagger\hat{A}(\omega)|x\rangle|^2. \quad (3)$$

Figure 1c display the quantum circuits designed for evaluating both terms in $L(\vec{\theta}_1)$, which have a depth at most equal to the sum of depths for $U_0(\vec{\theta}_0)$ and $U_1(\vec{\theta}_1)$, and do not involve any controlled operation on $U_0(\vec{\theta}_0)$ nor $U_1(\vec{\theta}_1)$ unlike in previous works [9, 10] (see the Methods section). This simplicity makes VQR more feasible for NISQ devices than those quantum algorithms requiring deep quantum circuits for computing response properties [8, 14, 29, 30]. Once $\vec{\theta}_1^{\text{opt}}$ have been found, $\chi(\omega)$ can be computed from

$$\chi(\omega) = \langle x | \hat{A}^\dagger(\omega) | x \rangle \frac{\langle \Psi_0 | \hat{V}^\dagger \hat{V} | \Psi_0 \rangle}{\langle x | \hat{A}^\dagger(\omega) \hat{A}(\omega) | x \rangle}, \quad (4)$$

by measuring the individual expectation value on quantum computers. To mitigate the impact of noises on NISQ devices, we further introduce a simple EM strategy based on symmetry projection to remove the unphysical components in a quantum state ($|\Psi_0\rangle$ or $|x\rangle$) caused by noises (see the Methods section). This yields a more accurate estimation for expectation values such as $\langle x | \hat{A}^\dagger(\omega) \hat{A}(\omega) | x \rangle$, which is crucial for the accurate computation of $\chi(\omega)$.

The present VQR approach allows to directly compute spectra in an interested frequency region without explicitly addressing excited states. This is particularly advantageous in the region with a large density of states or a region of high energy such as the X-ray region. We implement it on a programmable superconducting quantum processor [16] (see Fig. 2a), which consists of 20 frequency-tunable transmon qubits connected via a central resonator. A special feature of this device is that the $\sqrt{\text{iSWAP}}_{i,j}$ gate can be realized between any pair of qubits Q_i and Q_j (see Supplementary Section 2). Fermion-to-qubit mappings used in the experiments for H_2 (or polyacenes) and CO are shown in Figs. 2b and 2c, respectively. As the first application of VQR, we employ PQC capable of encoding the exact ground or response state as variational ansätze, and perform numerical optimizations by scanning the entire parameter space. This allows us to focus on the limitation of VQR solely due to noises on NISQ devices. Extensions to the uses of low-depth wavefunction ansätze scalable for larger systems [22] and quantum

gradients for optimizations [34] are straightforward.

Benchmark: dynamic polarizabilities of H₂

Due to its conceptual simplicity, H₂ in a minimal basis set has become a test bed for new quantum algorithms [6, 15, 21–24]. We benchmark the feasibility of VQR by comparing the simulated $\chi(\omega)$ with the corresponding FCI results for H₂ at three bond lengths ($R = R_e$ [25], $2R_e$, and $3R_e$), which cover the weak, intermediate, and strong electron correlation regimes. We first compute the ground state using VQE [6, 7] with the PQC ansatz in Fig. 3a (see the Methods section). Figure 3b demonstrates that the EM strategy improves the VQE(raw) energies considerably, making the difference with the FCI reference on the order of chemical accuracy (see Supplementary Table 5). After optimizing the ground states, we compute $\chi(\omega)$ for $\hat{V} = \hat{z}$ and $\gamma = 0.1$ a.u. using VQR with the PQC in Fig. 3c for $|x(\theta_1)\rangle$ (see the Methods section). As shown in Fig. 3d, $\chi(\omega)$ computed using VQR(EM) agrees with the FCI reference in most of the studied frequency region at all the three geometries. In particular, the absorption peaks responsible for the transition from the ground state to the first singlet excited states $|^1\Psi_u\rangle = \frac{1}{\sqrt{2}}(|10\rangle + |01\rangle)$ are well-reproduced. Meanwhile, small deviations from the FCI results are observed at ω around 0.6, 0.1, and 0.0 a.u. for $R = R_e$, $2R_e$, and $3R_e$, respectively. These frequencies turn out to be exactly the position of the first triplet excited state at each geometry. In these regions, the two terms in $L(\theta_1)$ are very close to each other and the difference is on the order of γ^2 . Thus, the computation of $L(\theta_1)$ is prone to noises, such that the optimized angle θ_1^{opt} is less accurate (see Supplementary Fig. 9). Future improvements on quantum hardware are expected to resolve this problem.

For comparison, we also compute $\chi(\omega)$ using DFT, the method of choice for computing dynamic polarizabilities of large molecules [1], with three popular exchange-correlation (XC) functionals (see Supplementary Fig. 11). For clarity, only the results obtained from the

Hartree-Fock (HF) method, viewed as a special XC functional, in spin-restricted (RHF) and spin-unrestricted (UHF) variants are displayed in Fig. 3c. We find that while different XC functionals give comparable results close to the FCI reference at the equilibrium, their performances deteriorate rapidly towards bond dissociation, where the occupied σ_g orbital and the unoccupied σ_u orbital become nearly degenerate. Besides, it is interesting to see that even though the symmetry-breaking UHF provides a good energy at $R = 3R_e$, the computed $\chi(\omega)$ are qualitatively wrong. These results highlight the failure of DFT with approximate density functionals in computing response properties of strongly correlated systems, for which VQR may become a better alternative for large systems in future.

UV-Vis absorption spectra of polyacenes

Having established the feasibility of VQR on NISQ devices, we apply it to solve more challenging problems of potential technological importance. We exemplify this capability by simulating UV-Vis absorption spectra of polyacenes [40], which are made up of linearly fused benzene rings. Specifically, we simulate the first absorption band (the so-called 1L_a or p band [40]) due to the transition from the highest occupied molecular orbital (HOMO) to the lowest unoccupied molecular orbital (LUMO), which is the most relevant band for their applications as optoelectronic devices [41]. As qubit resources are very limited on NISQ devices, simulating the entire molecule is currently impossible for polyacenes. To overcome this problem, we combine VQR with the complete active space (CAS) model [42] (see Fig. 4a), in which only a selected number of electrons and orbitals are treated at the FCI level. For polyacenes including naphthalene, anthracene, tetracene, and pentacene (see Fig. 4b), we choose a minimal active space composed of HOMO and LUMO with two active electrons, denoted by CAS(2e,2o). Then, VQE and VQR are applied to the reduced problem, for which the same experimental settings for H_2 can be used. To take into account the missing dynamic electron correlation due to the active

space approximation, all the computed spectra $\sigma_{\text{abs}}(\omega)$ are shifted by -1.9 eV estimated using perturbation theory (see Supplementary Section 3.6.2). As shown in Fig. 4c, the FCI spectra reproduce the key feature of the experimental spectra for polyacenes [40], i.e., the remarkable red shift as the number of rings increases. The major difference is that the simulated spectra are not vibrationally resolved, as the effects of nuclear motions are neglected, which will be taken into account in future.

We find that the VQR(raw) spectra are less accurate compared with those for H_2 . Since a much smaller broadening parameter ($\gamma = 0.01$ a.u.) is used here for a better resolution in the UV-Vis region, the computation of the denominator in Eq. (4) is more sensitive to noises. Even in this case, the EM strategy leads to a remarkable agreement with the FCI spectra. For naphthalene, a small artificial peak around 2.3 eV is observed in the VQR(EM) spectrum, for the same problem found for H_2 . For the other three molecules, the excitation energies of the first triplet states are smaller than 1.5 eV, and hence the simulated UV-Vis absorption spectra are not impaired. Although not illustrated in this work, the VQR algorithm is also applicable to simulating emission spectra, provided the initial excited state is prepared on quantum computers, e.g., using the variational quantum deflation method [43]. In combination with more sophisticated methods for treating dynamic correlations and vibrational effects, we expect VQR to become a useful computational tool for studying photophysics and photochemistry of molecules.

X-ray absorption spectra of CO

The distinct advantage of VQR for directly simulating spectra in an interested energy window without computing all the excited states below makes it very attractive for applications in X-ray spectroscopies, which are widely utilized for probing local molecular and electronic structures, but remain challenging for theoretical prediction [44, 45]. We demonstrate the capability of VQR for simulating the carbon K-edge and oxygen K-edge absorption spectra of

CO, combined with a CAS(4e,3o) model including σ_{1s_O} , σ_{1s_C} , and π_x^* orbitals (see Fig. 5a). The ground state is well-approximated by the Hartree-Fock state, i.e., $|\Psi_0\rangle = U_0|0\rangle = |1111\rangle$ with $U_0 = X_0X_1X_2X_3$ (see Supplementary Section 4.1), such that VQE is unnecessary in this case. For $\hat{V} = \hat{x}$, a response state can be exactly parameterized by $|x(\theta, \phi)\rangle = U_1(\theta, \phi)|0\rangle = \cos \frac{\theta}{2} |^1\Psi_{\sigma_{1s_O} \rightarrow \pi_x^*}\rangle + \sin \frac{\theta}{2} e^{i\phi} |^1\Psi_{\sigma_{1s_C} \rightarrow \pi_x^*}\rangle$ with two free angles θ and ϕ , where $U_1(\theta, \phi)$ is the PQC in Fig. 5b and $|^1\Psi_{\sigma_{1s_O} \rightarrow \pi_x^*}\rangle$ ($|^1\Psi_{\sigma_{1s_C} \rightarrow \pi_x^*}\rangle$) represents the singlet excited state due to the transition from the core orbital σ_{1s_O} (σ_{1s_C}) to the unoccupied orbital π_x^* . Figure 5c shows that while the VQR(raw) spectrum is almost vanishing, the improvement by EM is dramatic, giving rise to two visible absorption peaks in the VQR(EM) spectrum. Compared with the above two-qubit simulations, the deviation of the VQR(EM) spectrum from the FCI reference is larger. To better understand the discrepancy, we also measure $\sigma_{\text{abs}}(\omega)$ at the ideal angles (θ^*, ϕ^*) at each frequency, labelled by VQR(EM*) in Fig. 5c. The absorption spectra in the region around 500 eV are improved, where the computation of the cost function $L(\theta, \phi)$ is prone to noises due to the proximity of the two terms (see Supplementary Section 4.4). However, the heights of the two absorption peaks are not improved by VQR(EM*). The comparison suggests that the larger deviation from the FCI spectrum is not due to the inaccuracy in the optimized angles, but the inaccuracy in experimental preparation of the quantum state $|x(\theta, \phi)\rangle$ with the quantum circuit in Fig. 5b, which makes the computation of the denominator in Eq. (4) less accurate even with the ideal angles (see Supplementary Fig. 15). We verify this by characterizing the output state $|x(\theta, \phi)\rangle$ using quantum state tomography [23] (QST) at two special points $(\theta, \phi) = (0, 0)$ and $(\theta, \phi) = (\pi, 0)$ (see Fig. 5d), which correspond to $|^1\Psi_{\sigma_{1s_O} \rightarrow \pi_x^*}\rangle$ and $|^1\Psi_{\sigma_{1s_C} \rightarrow \pi_x^*}\rangle$, respectively. The fidelity [23] $F(\rho_{\text{exp}}, |\Psi\rangle) = \sqrt{\langle \Psi | \rho_{\text{exp}} | \Psi \rangle}$ as a measure for the similarity between an experimental state ρ_{exp} and an ideal state $|\Psi\rangle$ is 0.783 (0.791) for $|^1\Psi_{\sigma_{1s_O} \rightarrow \pi_x^*}\rangle$ ($|^1\Psi_{\sigma_{1s_C} \rightarrow \pi_x^*}\rangle$). In comparison, F for the response state (see Fig. 3c) at the peak position of $\chi(\omega)$ for H_2 at $R = R_e$ is found as high as 0.991. The lowering of F can be attributed to the doubling of the number

of $\sqrt{i\text{SWAP}}$ gates and the lowering of gate fidelities (see the Methods section). Note that even though the peak height given by VQR(EM) is not ideal, the more important peak positions, which determine core excitation energies, are still reasonably good. The remaining discrepancy with the experimental core excitation energies [46,47] obtained from high-resolution photoabsorption spectra (dotted lines in Fig. 5c) can be improved by employing a larger active space and a better basis set in future. These multi-qubit results demonstrate that VQR can potentially scale up to larger systems on improved quantum hardware with higher two-qubit gate fidelities.

Discussion

The proposed VQR approach circumvents the requirement of deep quantum circuits in previous quantum algorithms [8, 14, 29, 30], and hence enables the first ever quantum simulation of linear optical properties of molecules on a superconducting quantum processor. In particular, we demonstrate a feasible and universal algorithmic primitive for solving the linear response equation on NISQ devices, which can be easily extended to simulate other properties such as Green’s functions and nonlinear response properties. The VQR approach is not limited to superconducting devices, but also applicable to other quantum computing platforms. With the advent of more powerful large-scale quantum processors with lower error rates, we anticipate wide application of this general approach in simulating response properties of more complex molecules and condense-phase systems in the near future.

Our work has opened up the possibility of identifying a practical quantum computational advantage in simulating molecular response properties on NISQ devices. Compared with classical computers, quantum computers naturally have a storage advantage in representing quantum states with a computational resource that grows only linearly instead of exponentially with the molecular size, which has been utilized in the proposed hybrid quantum-classical approach. Our simulation results suggest that a potential computational advantage over standard methods

on classical computers may exist in the strong electron correlation regime, for which VQR may provide an accurate and efficient solution when combined with the CAS model and EM techniques. Important applications in this category include simulating spectra for challenging systems involving transition metals such as high-temperature superconductors. For large systems, such advantage also crucially hinges on the variational ansatz [6, 7, 22, 48] and the magnitude of noises in multi-qubit cases, as indicated by the four-qubit VQR experiments for CO. We emphasize that all these factors need to be carefully studied in future, in order to firmly establish a transformative computational tool for designing new materials with specific properties.

Methods

VQR with EM The VQR algorithm for linear response properties of molecules includes two steps: obtaining the response state $|x\rangle$ at a given frequency ω by minimizing $L(\vec{\theta}_1)$ in Eq. (3) and measuring $\chi(\omega)$ using Eq. (4). The expectation value $\langle x|\hat{A}^\dagger(\omega)\hat{A}(\omega)|x\rangle$ in $L(\vec{\theta}_1)$ is computed by preparing $|x\rangle$ on quantum processors and performing projective measurements to obtain $\langle x|P_k|x\rangle$ for each P_k in $\hat{A}^\dagger(\omega)\hat{A}(\omega)$, which is achieved by adding appropriate single-qubit rotations (I , $X_{-\pi/2}$ or $Y_{\pi/2}$) for polarizations along different axes before measurements. The cross term $|\langle\Psi_0|\hat{V}^\dagger\hat{A}(\omega)|x\rangle|^2$ is more involved. Let $\hat{V}^\dagger\hat{A}(\omega) = \sum_k c_k(\omega)P_k$, we have $|\langle\Psi_0|\hat{V}^\dagger\hat{A}(\omega)|x\rangle|^2 = \sum_{lk} \bar{c}_l(\omega)c_k(\omega)\langle 0|U_1^\dagger P_l U_0|0\rangle\langle 0|U_0^\dagger P_k U_1|0\rangle$. We design a quantum circuit shown in Fig. 1c for evaluating $\langle 0|U_1^\dagger P_l U_0|0\rangle\langle 0|U_0^\dagger P_k U_1|0\rangle$. For special $\hat{V}^\dagger\hat{A}(\omega)$ in this work, the evaluation of $|\langle\Psi_0|\hat{V}^\dagger\hat{A}(\omega)|x\rangle|^2$ is further reduced using symmetries to quantum circuits without involving the ancilla qubit and controlled Pauli operators (see Supplementary Section 1.2 in detail). The working expression Eq. (4) for $\chi(\omega)$ is derived from its definition in Eq. (23) (see Supplementary Section 1.1). Shapes of $\sigma_{\text{abs}}(\omega)$ can be understood by noting that $\text{Im}\chi(\omega)$ is a superposition of Lorentzians with a common full width at half maximum (FWHM) 2γ , viz., $\text{Im}\chi(\omega) = \sum_n |\langle\Psi_n|\hat{V}|\Psi_0\rangle|^2 \frac{\gamma}{(\omega_{n0}-\omega)^2+\gamma^2}$. Further details of the VQR approach are in

Supplementary Section 1.

The EM strategy based on symmetry projection works as follows. If a quantum state $|\Psi\rangle$ (ground or response state) resides in a subspace with spatial or spin symmetry, a projector \mathcal{P} can be associated with this subspace such that $\mathcal{P}|\Psi\rangle = |\Psi\rangle$. In the presence of noises in experiments, the quantum system needs to be described a density matrix [23] ρ_{exp} instead of $|\Psi\rangle$, which can have undesirable components outside the correct subspace. To get a better estimation of the expectation value $\langle\Psi|\hat{O}|\Psi\rangle$ for an operator \hat{O} that commutes with \mathcal{P} (e.g., \hat{H}_0 , $\hat{A}(\omega)$, $\hat{A}^\dagger(\omega)\hat{A}(\omega)$, and $\hat{V}^\dagger\hat{V}$), we can use $\langle\Psi|\hat{O}|\Psi\rangle^{\text{EM}} \equiv \text{tr}(\tilde{\rho}\hat{O}) = \text{tr}(\rho_{\text{exp}}\hat{O}\mathcal{P})/\text{tr}(\rho_{\text{exp}}\mathcal{P})$ with $\tilde{\rho} = \mathcal{P}\rho_{\text{exp}}\mathcal{P}/\text{tr}(\rho_{\text{exp}}\mathcal{P})$ being the projected density matrix. This EM strategy may require a small amount of additional measurements for computing the expectation values of $\hat{O}\mathcal{P}$ and \mathcal{P} . The choice of \mathcal{P} for different problems is presented below.

Device information The qubits (Q_3 , Q_6 , Q_{13} , Q_{14} , and Q_{20}) used in our experiments are selected based on the decoherence time and the coupling strength g_i between a qubit Q_i and the bus resonator. Longer decoherence time will enable more accurate basic qubit operations, while larger g_i can improve the effective coupling strength between qubits mediated by the bus resonator, and hence reduces the characteristic time of the two-qubit gate. Qubit frequencies are carefully arranged to minimize unwanted interactions and crosstalk errors among qubits during single-qubit operations. Each qubit has its own flux bias line for Z rotations $Z_\theta = e^{-i\frac{\theta}{2}Z}$, which are realized by amplitude-adjustable Z square pulses with a width of 20 ns. The four qubits (Q_3 , Q_6 , Q_{13} , and Q_{20}) have their own microwave control lines for implementing XY rotations ($X_\theta = e^{-i\frac{\theta}{2}X}$ or $Y_\theta = e^{-i\frac{\theta}{2}Y}$), while for the qubit Q_{14} the Z-control line is shared by XY and Z signals (see Fig. 2a), which are combined at room temperature by a directional coupler. Each qubit is dispersively coupled to its own readout resonator for measuring qubit states, and all the qubits can be measured simultaneously using the frequency-domain multiplexing technique. The $\sqrt{\text{iSWAP}}$ gate is generated by tuning the involved qubits on-resonance but detuned from

the bus resonator in frequency after certain evolution time $t_{\sqrt{\text{iSWAP}}}$ (see Supplementary Section 2.3). Two-qubit gate fidelities characterized by quantum process tomography are 0.9806, 0.9766, 0.9679, and 0.9508 for Q₁₄-Q₂₀, Q₃-Q₆, Q₃-Q₁₃, and Q₆-Q₂₀, respectively. More detailed information about the device and experimental setup can be found in Supplementary Section 2.

Two-qubit simulations for H₂ and polyacenes For H₂ in the STO-3G basis, the Bravyi-Kitaev mapping [4, 5] with the Z_2 reduction [28] leads to a mapping of occupation number vectors (ONVs) shown in Fig. 2b, i.e., $|n_0 n_1 n_2 n_3\rangle = |n_{\sigma_g^\alpha} n_{\sigma_u^\alpha} n_{\sigma_g^\beta} n_{\sigma_u^\beta}\rangle \rightarrow |q_0 q_1\rangle = |n_0 n_2\rangle$, where $n_i \in \{0, 1\}$ is the occupation number of a spin-orbital, $q_i \in \{0, 1\}$ is the status of a qubit, and the symbol g (u) refers to the RHF molecular orbital with gerade (ungerade) symmetry. The resulting Hamiltonian and perturbation operator are $\hat{H}_0 = h_0 I + h_1 Z_0 + h_2 Z_1 + h_3 Z_0 Z_1 + h_4 X_0 X_1$ and $\hat{V} = v_0 (X_0 + X_1)$, respectively, where the coefficients h_i and v_0 are obtained using the PySCF package [29]. The quantum circuit in Fig. 3a gives a parameterized quantum state $|\Psi(\theta_0)\rangle = U_0(\theta_0)|0\rangle = \cos \frac{\theta_0}{2}|11\rangle + \sin \frac{\theta_0}{2}|00\rangle$ up to an irrelevant global phase, while that in Fig. 3b leads to $|x(\theta_1)\rangle = U_1(\theta_1)|0\rangle = \cos \frac{\theta_1}{2}|10\rangle + \sin \frac{\theta_1}{2}|01\rangle$ up to a global phase. The spatial symmetry projectors used in EM are $\mathcal{P}_g = |00\rangle\langle 00| + |11\rangle\langle 11| = \frac{1}{2}(I + Z_0 Z_1)$ and $\mathcal{P}_u = |01\rangle\langle 01| + |10\rangle\langle 10| = \frac{1}{2}(I - Z_0 Z_1)$ for $|\Psi(\theta_0)\rangle$ and $|x(\theta_1)\rangle$, respectively. The CAS(2e,2o) model for polyacenes can be described in the same settings. Details of the quantum circuit for computing $|\langle \Psi_0 | \hat{V}^\dagger \hat{A}(\omega) | x \rangle|^2$, formulae for EM, measured results for individual terms, and optimizations for $L(\theta_1)$ can be found in Supplementary Section 3.

Four-qubit simulations for CO For the CAS(4e,3o) model of CO, the parity mapping [5] with the Z_2 reduction [4] leads to a mapping of ONVs shown in Fig. 2c, i.e., $|n_0 n_1 n_2 n_3 n_4 n_5\rangle = |n_{\sigma_{1s_O}^\alpha} n_{\pi_x^{\alpha*}} n_{\sigma_{1s_C}^\alpha} n_{\sigma_{1s_O}^\beta} n_{\pi_x^{\beta*}} n_{\sigma_{1s_C}^\beta}\rangle \rightarrow |q_0 q_1 q_2 q_3\rangle = |n_0(n_0 + n_1 \bmod 2)n_3(n_3 + n_4 \bmod 2)\rangle$. Consequently, the Hartree-Fock state becomes $|\Psi_0\rangle = |1111\rangle = U_0|0\rangle$ with $U_0 = X_0 X_1 X_2 X_3$, and the singlet excited states are $|^1\Psi_{\sigma_{1s_O} \rightarrow \pi_x^*}\rangle = \frac{1}{\sqrt{2}}(|0111\rangle + |1101\rangle)$ and $|^1\Psi_{\sigma_{1s_C} \rightarrow \pi_x^*}\rangle =$

$\frac{1}{\sqrt{2}}(|1011\rangle + |1110\rangle)$, respectively. The active space Hamiltonian can be well-approximated by $\hat{H}_0 = \sum_{k=0}^{15} h_k P_k$ with $P_k \in \{I, Z\}^{\otimes 4}$, and the perturbation operator is $\hat{V} = v_0(X_0 + X_2) + v_1(X_1 + X_3)$. The spin symmetry projector used in EM for $|x(\theta, \phi)\rangle$ is $\mathcal{P}_S = \mathcal{P}_S^O + \mathcal{P}_S^C$ with $\mathcal{P}_S^O = \frac{1}{2}(|0111\rangle + |1101\rangle)(\langle 0111| + \langle 1101|) = \frac{1}{16}(I - Z_0 Z_2 + X_0 X_2 + Y_0 Y_2)(I - Z_1)(I - Z_3)$ and $\mathcal{P}_S^C = \frac{1}{2}(|1011\rangle + |1110\rangle)(\langle 1011| + \langle 1110|) = \frac{1}{16}(I - Z_1 Z_3 + X_1 X_3 + Y_1 Y_3)(I - Z_0)(I - Z_2)$. Details of the quantum circuits for computing $|\langle \Psi_0 | \hat{V}^\dagger \hat{A}(\omega) | x \rangle|^2$, formulae for EM, landscapes of individual terms in $L(\theta, \phi)$, and optimization results can be found in Supplementary Section 4.

Data availability

All data supporting the findings of this study are available within the paper and the Supplementary Information.

References

- [1] Marzari, N., Ferretti, A. & Wolverton, C. Electronic-structure methods for materials design. *Nat. Mater.* **20**, 736–749 (2021).
- [2] Helgaker, T. *et al.* Recent advances in wave function-based methods of molecular-property calculations. *Chem. Rev.* **112**, 543–631 (2012).
- [3] Norman, P., Ruud, K. & Saue, T. *Principles and practices of molecular properties: Theory, modeling, and simulations* (John Wiley & Sons, 2018).
- [4] Cohen, A. J., Mori-Sánchez, P. & Yang, W. Insights into current limitations of density functional theory. *Science* **321**, 792–794 (2008).

- [5] Feynman, R. P. Simulating physics with computers. *Int. J. Theor. Phys.* **21**, 467–488 (1982).
- [6] Arute, F. *et al.* Quantum supremacy using a programmable superconducting processor. *Nature* **574**, 505–510 (2019).
- [7] Wu, Y. *et al.* Strong quantum computational advantage using a superconducting quantum processor. *Phys. Rev. Lett.* **127**, 180501 (2021).
- [8] Preskill, J. Quantum computing in the nisq era and beyond. *Quantum* **2**, 79 (2018).
- [9] Cao, Y. *et al.* Quantum chemistry in the age of quantum computing. *Chem. Rev.* **119**, 10856–10915 (2019).
- [10] McArdle, S., Endo, S., Aspuru-Guzik, A., Benjamin, S. C. & Yuan, X. Quantum computational chemistry. *Rev. Mod. Phys.* **92**, 015003 (2020).
- [11] Bauer, B., Bravyi, S., Motta, M. & Chan, G. K.-L. Quantum algorithms for quantum chemistry and quantum materials science. *Chem. Rev.* **120**, 12685–12717 (2020).
- [12] Reiher, M., Wiebe, N., Svore, K. M., Wecker, D. & Troyer, M. Elucidating reaction mechanisms on quantum computers. *Proc. Natl. Acad. Sci. U.S.A.* **114**, 7555–7560 (2017).
- [13] Li, Z., Li, J., Dattani, N. S., Umrigar, C. & Chan, G. K.-L. The electronic complexity of the ground-state of the fmo cofactor of nitrogenase as relevant to quantum simulations. *J. Chem. Phys.* **150**, 024302 (2019).
- [14] Aspuru-Guzik, A., Dutoi, A. D., Love, P. J. & Head-Gordon, M. Simulated quantum computation of molecular energies. *Science* **309**, 1704–1707 (2005).

- [15] Lanyon, B. P. *et al.* Towards quantum chemistry on a quantum computer. *Nat. Chem.* **2**, 106 (2010).
- [16] Whitfield, J. D., Biamonte, J. & Aspuru-Guzik, A. Simulation of electronic structure hamiltonians using quantum computers. *Mol. Phys.* **109**, 735–750 (2011).
- [17] Peruzzo, A. *et al.* A variational eigenvalue solver on a photonic quantum processor. *Nat. Commun.* **5**, 4213 (2014).
- [18] McClean, J. R., Romero, J., Babbush, R. & Aspuru-Guzik, A. The theory of variational hybrid quantum-classical algorithms. *New J. Phys.* **18**, 023023 (2016).
- [19] Cerezo, M. *et al.* Variational quantum algorithms. *Nat. Rev. Phys.* 1–20 (2021).
- [20] Kitaev, A. Y. Quantum measurements and the abelian stabilizer problem. *arXiv preprint quant-ph/9511026* (1995).
- [21] O’Malley, P. J. *et al.* Scalable quantum simulation of molecular energies. *Phys. Rev. X* **6**, 031007 (2016).
- [22] Kandala, A. *et al.* Hardware-efficient variational quantum eigensolver for small molecules and quantum magnets. *Nature* **549**, 242 (2017).
- [23] Hempel, C. *et al.* Quantum chemistry calculations on a trapped-ion quantum simulator. *Phys. Rev. X* **8**, 031022 (2018).
- [24] Sagastizabal, R. *et al.* Experimental error mitigation via symmetry verification in a variational quantum eigensolver. *Phys. Rev. A* **100**, 010302 (2019).
- [25] Rice, J. E. *et al.* Quantum computation of dominant products in lithium–sulfur batteries. *J. Chem. Phys.* **154**, 134115 (2021).

- [26] Arute, F. *et al.* Hartree-fock on a superconducting qubit quantum computer. *Science* **369**, 1084–1089 (2020).
- [27] Nielsen, M. A. & Chuang, I. L. *Quantum computation and quantum information* (Cambridge University Press, 2010).
- [28] Somma, R., Ortiz, G., Gubernatis, J. E., Knill, E. & Laflamme, R. Simulating physical phenomena by quantum networks. *Phys. Rev. A* **65**, 042323 (2002).
- [29] Chiesa, A. *et al.* Quantum hardware simulating four-dimensional inelastic neutron scattering. *Nat. Phys.* **15**, 455–459 (2019).
- [30] Sun, S.-N. *et al.* Quantum computation of finite-temperature static and dynamical properties of spin systems using quantum imaginary time evolution. *PRX Quantum* **2**, 010317 (2021).
- [31] Cai, X., Fang, W.-H., Fan, H. & Li, Z. Quantum computation of molecular response properties. *Phys. Rev. Res.* **2**, 033324 (2020).
- [32] Harrow, A. W., Hassidim, A. & Lloyd, S. Quantum algorithm for linear systems of equations. *Phys. Rev. Lett.* **103**, 150502 (2009).
- [33] Song, C. *et al.* Generation of multicomponent atomic schrödinger cat states of up to 20 qubits. *Science* **365**, 574–577 (2019).
- [34] Haug, K. *et al.* Quantum generative adversarial networks with multiple superconducting qubits. *npj Quantum Inf.* **5**, 1–5 (2021).
- [35] Bravyi, S. & Kitaev, A. Y. Fermionic quantum computation. *Ann. Phys.* **298**, 210–226 (2002).

- [36] Seeley, J. T., Richard, M. J. & Love, P. J. The bravyi-kitaev transformation for quantum computation of electronic structure. *J. Chem. Phys.* **137**, 224109 (2012).
- [37] Xu, X. *et al.* Variational algorithms for linear algebra. *arXiv preprint arXiv:1909.03898* (2019).
- [38] Bravo-Prieto, C. *et al.* Variational quantum linear solver. *arXiv preprint arXiv:1909.05820* (2019).
- [39] Huber, K. P. & Herzberg, G. *Molecular Spectra and Molecular Structure IV. Constants of Diatomic Molecules* (Van Nostrand Reinhold, New York, 1979).
- [40] Clar, E. & Schoental, R. *Polycyclic hydrocarbons*, vol. 1 (Springer, 1964).
- [41] Anthony, J. E. Functionalized acenes and heteroacenes for organic electronics. *Chem. Rev.* **106**, 5028–5048 (2006).
- [42] Szalay, P. G., Muller, T., Gidofalvi, G., Lischka, H. & Shepard, R. Multiconfiguration self-consistent field and multireference configuration interaction methods and applications. *Chem. Rev.* **112**, 108–181 (2012).
- [43] Higgott, O., Wang, D. & Brierley, S. Variational quantum computation of excited states. *Quantum* **3**, 156 (2019).
- [44] Norman, P. & Dreuw, A. Simulating x-ray spectroscopies and calculating core-excited states of molecules. *Chem. Rev.* **118**, 7208–7248 (2018).
- [45] Besley, N. A. Modeling of the spectroscopy of core electrons with density functional theory. *Wiley Interdiscip. Rev. Comput. Mol. Sci.* e1527 (2021).

- [46] Ma, Y., Chen, C., Meigs, G., Randall, K. & Sette, F. High-resolution k-shell photoabsorption measurements of simple molecules. *Phys. Rev. A* **44**, 1848 (1991).
- [47] Püttner, R. *et al.* Vibrationally resolved o 1s core-excitation spectra of co and no. *Phys. Rev. A* **59**, 3415 (1999).
- [48] McClean, J. R., Boixo, S., Smelyanskiy, V. N., Babbush, R. & Neven, H. Barren plateaus in quantum neural network training landscapes. *Nat. Commun.* **9**, 1–6 (2018).
- [49] Bravyi, S., Gambetta, J. M., Mezzacapo, A. & Temme, K. Tapering off qubits to simulate fermionic hamiltonians. *arXiv preprint arXiv:1701.08213* (2017).
- [50] Sun, Q. *et al.* Pyscf: the python-based simulations of chemistry framework. *Wiley Interdiscip. Rev. Comput. Mol. Sci.* **8**, e1340 (2018).

Acknowledgments

This work was supported by the National Natural Science Foundation of China (Grant Nos. 21973003, 21688102, T2121001, 11934018, 11904393, 92065114 and 12174207), the Strategic Priority Research Program of Chinese Academy of Sciences (Grant Nos. XDB28000000) and the Beijing Natural Science Foundation (Z2000009).

Author contributions

Z.L. and X.C. designed the study. K.H. and H.L. conducted the experiments, supervised by Z.B.L., K.X. and F.H.. K.H., X.C., Z.Y.G., H.L. and R.H. performed the numerical simulations. K.H., H.L., T.L., Y.S. and C.C. participated in the development of measurement and control system. H.K.L. and D.Z. fabricated the device. K.H., X.C., H.L., K.X., Z.L., H.F. and W.H.F.

cowrote the manuscript. All authors contributed to the discussion of the results and development of the manuscript.

Competing interests

Authors declare no competing interests.

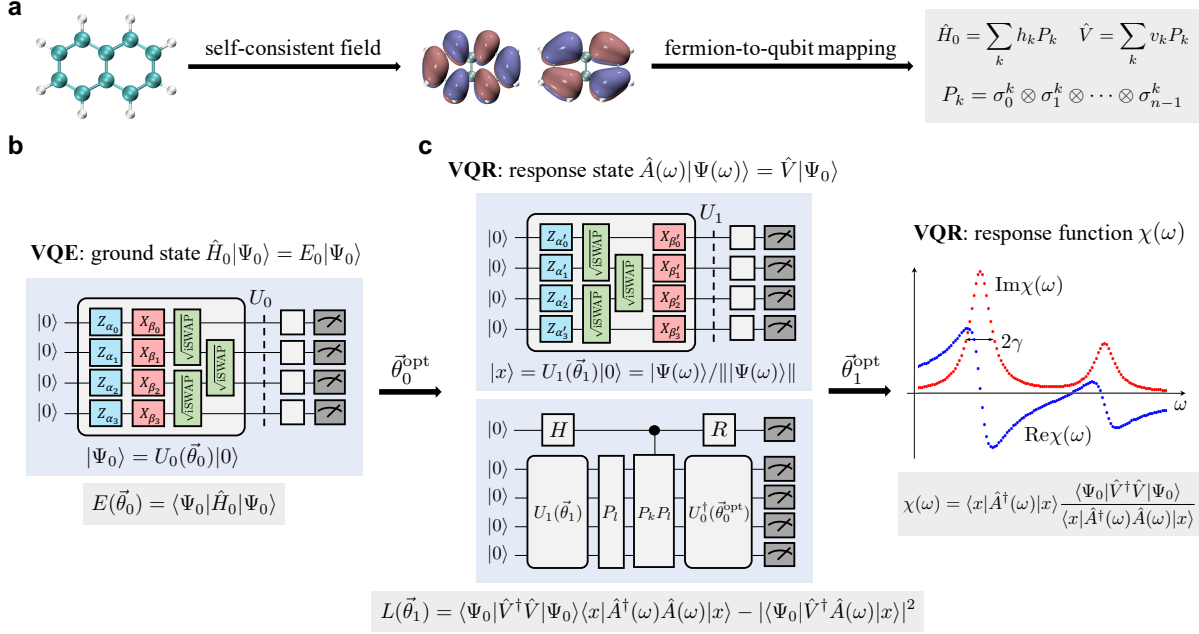


Figure 1: Quantum computational strategy for linear response properties of molecules.

a, Preprocessing step on classical computers. For a given molecule, an initial set of molecular orbitals is prepared from self-consistent field calculations, after which a fermion-to-qubit mapping is employed to transform \hat{H}_0 and \hat{V} to their counterparts for n qubits represented by linear combinations of Pauli terms P_k . **b**, VQE for preparing the ground state. A wavefunction ansatz is defined for $|\Psi_0\rangle = U_0(\vec{\theta}_0)|0\rangle$, where $U_0(\vec{\theta}_0)$ is a PQC with a set of variational parameters $\vec{\theta}_0$, usually composed of parameterized single-qubit rotations (e.g., Z_{α_k} and X_{β_l}) and two-qubit entangling gates (e.g., $\sqrt{i}\text{SWAP}$). The optimized parameters $\vec{\theta}_0^{\text{opt}}$ are found by minimizing the energy function $E(\vec{\theta}_0)$ on classical computers, with the necessary expectation values $\langle\Psi_0|P_k|\Psi_0\rangle$ computed using the presented quantum circuit on quantum computers. **c**, VQR for linear response properties. Given a frequency ω in an interested energy window and a broadening parameter γ for controlling the width of the computed spectra as input, the linear response equation is first solved by minimizing a cost function $L(\vec{\theta}_1)$ with a PQC for the normalized response state $|x\rangle = U_1(\vec{\theta}_1)|0\rangle = |\Psi(\omega)\rangle / \|\Psi(\omega)\rangle\|$. The term $\langle x|\hat{A}^\dagger(\omega)\hat{A}(\omega)|x\rangle$ is computed using the upper quantum circuit in a similar way as the energy, and the cross term $|\langle\Psi_0|\hat{V}^\dagger\hat{A}(\omega)|x\rangle|^2$ can be evaluated using the lower quantum circuit (see the Methods section), whose depth is mainly determined by the sum of depths for U_0 and U_1 . Once $\vec{\theta}_1^{\text{opt}}$ is obtained, the response function $\chi(\omega)$ at the specific ω is computed by measuring expectation values in Eq. (4) on quantum computers.

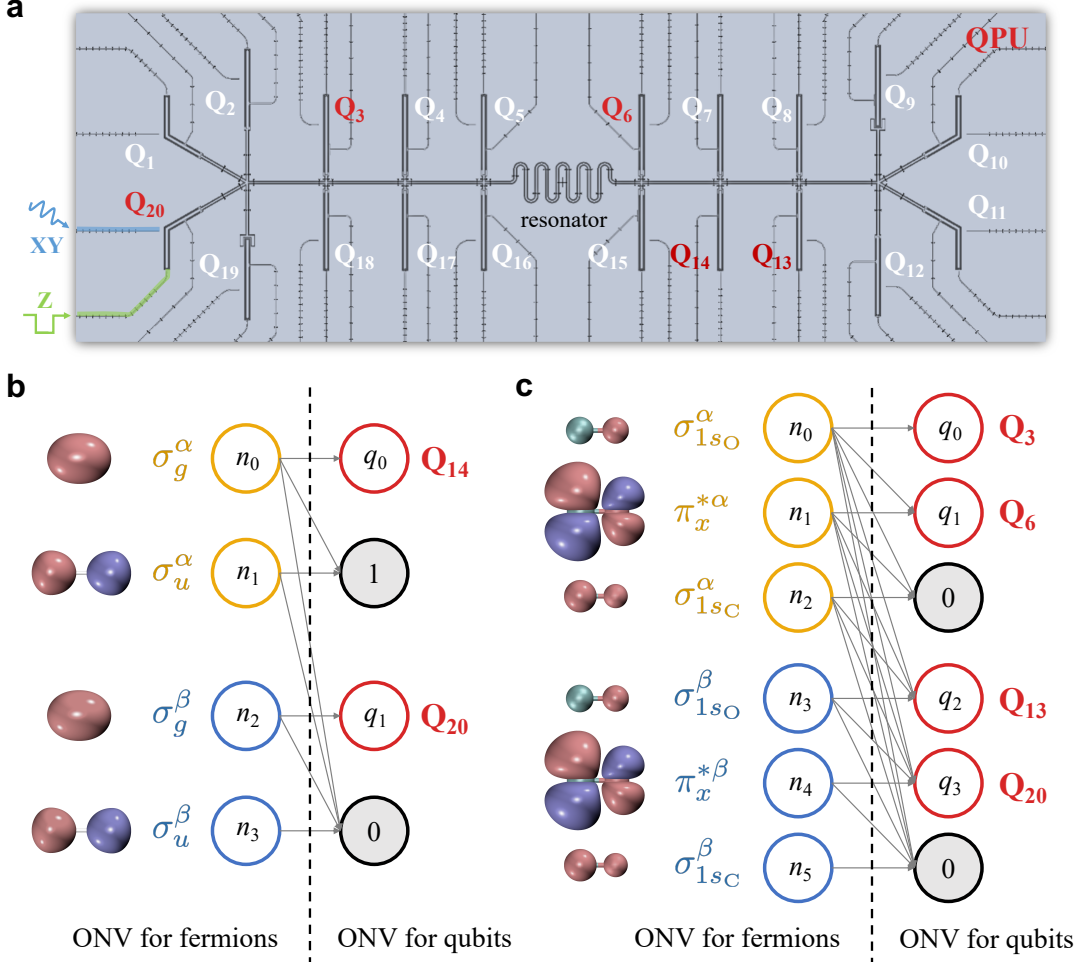


Figure 2: **Quantum processor unit (QPU) and fermion-to-qubit mappings.** **a**, False-color optical micrograph of the 20-qubit superconducting quantum device, with qubits used in experiments (red), unused qubits (white), the bus resonator (black), qubit XY-control lines (blue), and Z-control lines (green) highlighted. **b**, The Bravyi-Kitaev mapping [4, 5] with the Z_2 reduction [28] used in the simulations of H_2 in a minimal basis set and polyacenes within a CAS(2e,2o) model for transforming the occupation number vectors (ONVs) for fermions $|n_0 n_1 n_2 n_3\rangle = |n_{\sigma_g^\alpha} n_{\sigma_u^\alpha} n_{\sigma_g^\beta} n_{\sigma_u^\beta}\rangle$ ($n \in \{0, 1\}$) to the ONVs for two qubits $|q_0 q_1\rangle = |n_0 n_2\rangle$. **c**, The parity mapping [5] with the Z_2 reduction [28] used in the simulation of CO within a CAS(4e,3o) model for transforming the ONVs for fermions $|n_0 n_1 n_2 n_3 n_4 n_5\rangle = |n_{\sigma_{1sO}^\alpha} n_{\pi_x^{*\alpha}} n_{\sigma_{1sC}^\alpha} n_{\sigma_{1sO}^\beta} n_{\pi_x^{*\beta}} n_{\sigma_{1sC}^\beta}\rangle$ to the ONVs for four qubits $|q_0 q_1 q_2 q_3\rangle = |n_0 (n_0 + n_1 \bmod 2) n_3 (n_3 + n_4 \bmod 2)\rangle$. The grey arrows going into the same qubit indicate the sum of the input occupation numbers modulo two. In both cases, the conservation of the total number of electrons and the spin projection gives rise to two reducible qubits (grey circles) with constant status (referred as the Z_2 reduction [28]).

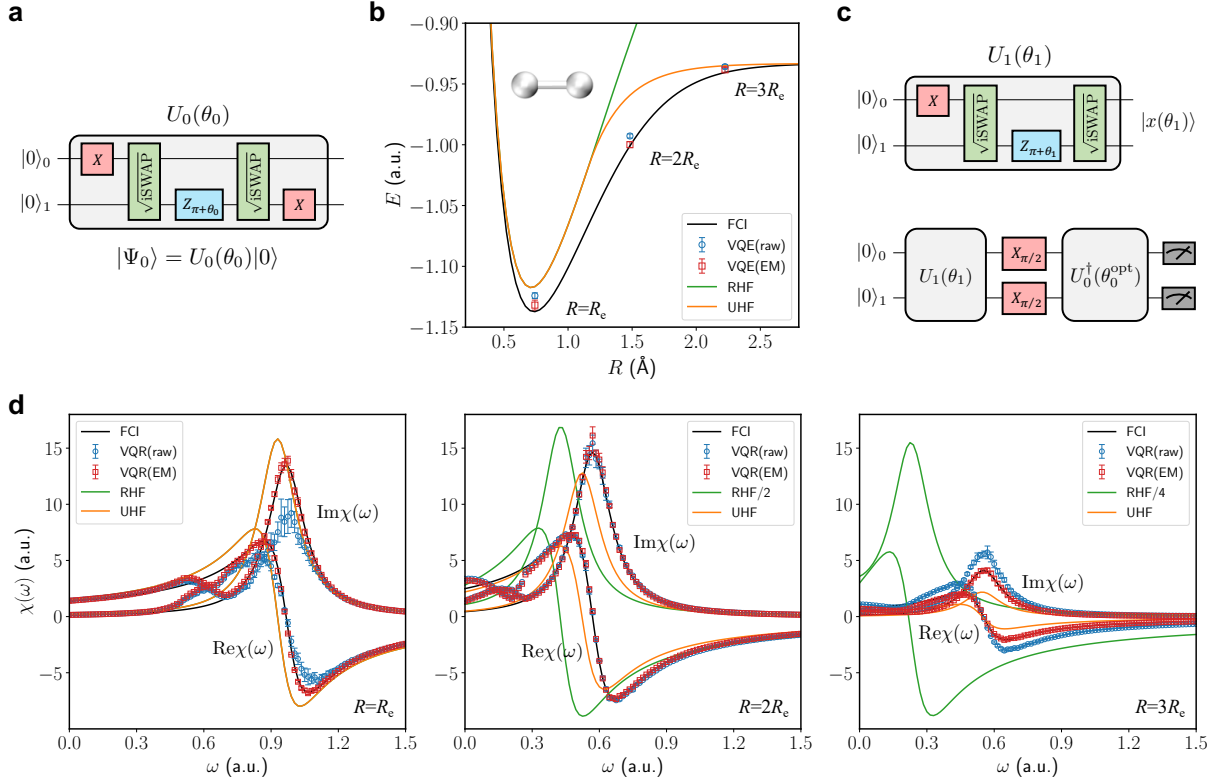


Figure 3: Ground-state energies and dipole polarizabilities of H_2 from two-qubit simulations. **a**, PQC for the ground state $|\Psi_0(\theta_0)\rangle$ in VQE. **b**, Ground-state energies obtained by VQE (blue circles for raw results and red squares for error mitigated results) at three bond distances, i.e., R_e (the experimental equilibrium bond distance), $2R_e$, and $3R_e$. For comparison, the potential energy curves obtained from FCI (black), RHF (green) and UHF (orange) are also displayed. **c**, PQC for the response state $|x(\theta_1)\rangle$ in VQR (upper) and the quantum circuit used for evaluating the cross term $|\langle\Psi_0|\hat{V}^\dagger\hat{A}(\omega)|x\rangle|^2$ (lower), see Supplementary Section 3.2. **d**, Real and imaginary parts of $\chi(\omega)$ computed with $\gamma = 0.1$ a.u. at three different geometries. Note that the RHF spectrum coincides with the UHF spectrum at $R = R_e$, while those at $R = 2R_e$ and $R = 3R_e$ are scaled by 1/2 and 1/4, respectively, in order to fit into the same figure.

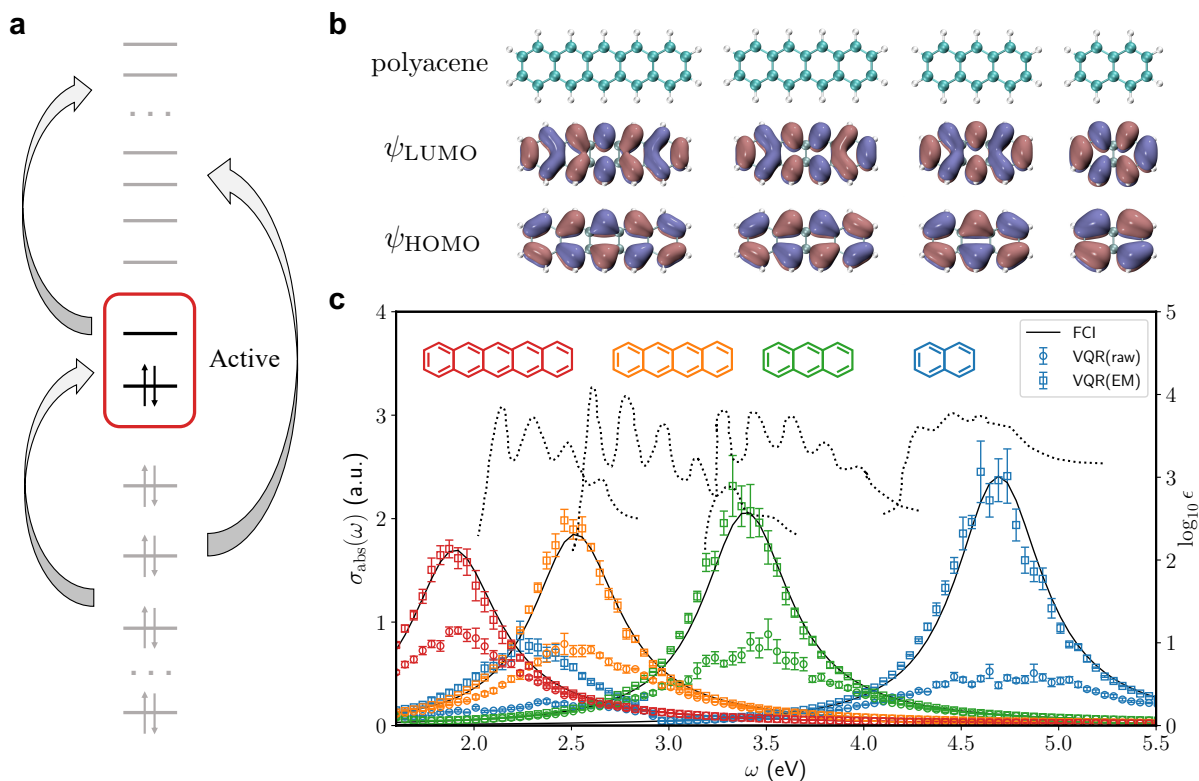


Figure 4: **UV-Vis absorption spectra of polyacenes from two-qubit simulations.** **a**, Active space model in which only a selected number of electrons and orbitals within the active space (red box) are treated at the FCI level. Grey arrows represent excitations responsible for dynamic electron correlation missed by the active space approximation. **b**, Structures of the polyacenes with different number of rings ($n = 2, 3, 4, 5$) and the CAS(2e,2o) model composed of HOMO and LUMO for each molecule. **c**, Simulated absorption spectra $\sigma_{\text{abs}}(\omega)$ with $\gamma = 0.01$ a.u. (open circles for raw results and squares for error mitigated results) compared against the FCI results (black lines). All the computed spectra have been shifted by -1.9 eV to take into account the missing dynamic correlation. The experimental absorption spectra (dotted lines) are taken from Ref. [40].

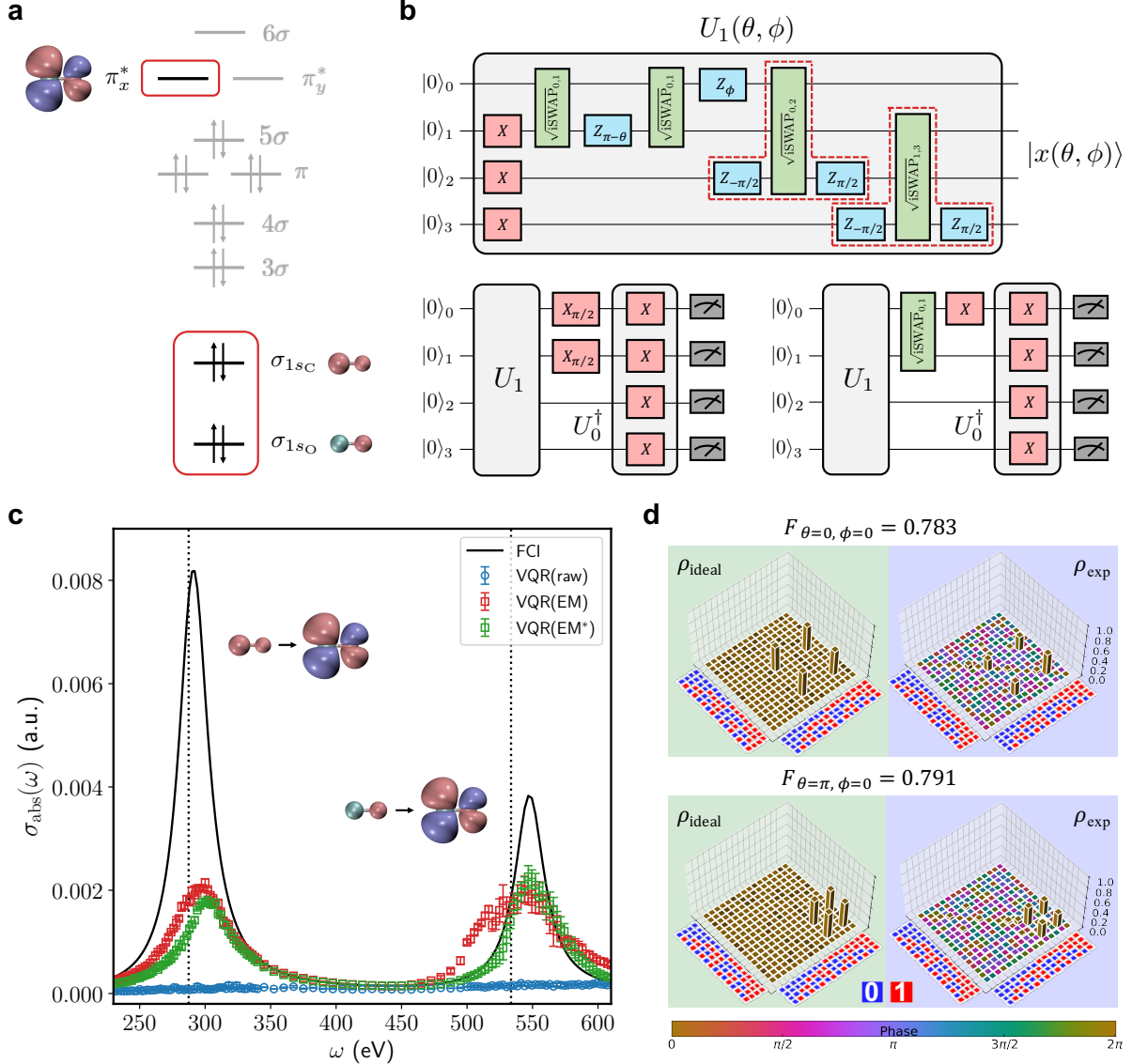


Figure 5: X-ray absorption spectra of CO from four-qubit simulations. **a**, Molecular orbital diagram and the CAS(4e,3o) model composed of σ_{1sO} , σ_{1sC} , and π_x^* orbitals (red boxes). **b**, PQC for $|x(\theta, \phi)\rangle$ in VQR (upper) and the two quantum circuits for evaluating the cross term $|\langle \Psi_0 | \hat{V}^\dagger \hat{A}(\omega) | x \rangle|^2$ (lower), see Supplementary Section 4.2. **c**, Simulated absorption spectra $\sigma_{\text{abs}}(\omega)$ with $\gamma = 0.5$ a.u. (open circles for raw results and squares for error mitigated results) in comparison with the FCI results (black lines). The VQR(EM*) results are measured at the ideal angles (θ^*, ϕ^*) at each frequency. Vertical dotted lines indicate the positions of core excitation energies determined from high-resolution photoabsorption spectra [46, 47]. **d**, Experimental density matrices ρ_{exp} characterized by QST for $|x(\theta, \phi)\rangle$ at two special points $(\theta, \phi) = (0, 0)$ and $(\theta, \phi) = (\pi, 0)$, which correspond to $|^1\Psi_{\sigma_{1sO} \rightarrow \pi_x^*}\rangle$ and $|^1\Psi_{\sigma_{1sC} \rightarrow \pi_x^*}\rangle$, respectively. The ideal density matrix $\rho_{\text{ideal}} = |\Psi\rangle\langle\Psi|$ (with $|\Psi\rangle$ being $|^1\Psi_{\sigma_{1sO} \rightarrow \pi_x^*}\rangle$ or $|^1\Psi_{\sigma_{1sC} \rightarrow \pi_x^*}\rangle$) and the fidelity [23] $F(\rho_{\text{exp}}, \rho_{\text{ideal}})$ are also shown for comparison.

Supplementary Information: Simulating linear optical properties of molecules on a superconducting quantum processor

Kaixuan Huang^{2,3†}, Xiaoxia Cai^{1†}, Hao Li^{3,7†}, Zi-Yong Ge⁵, Ruijuan Hou¹, Hekang Li³, Tong Liu^{3,4}, Yunhao Shi^{3,4}, Chitong Chen^{3,4}, Dongning Zheng^{3,4,6}, Kai Xu^{3,4,6*}, Zhi-Bo Liu^{2*}, Zhendong Li^{1*}, Heng Fan^{3,4,6*}, Wei-Hai Fang¹

¹ Key Laboratory of Theoretical and Computational Photochemistry, Ministry of Education, College of Chemistry, Beijing Normal University, Beijing 100875, China

² The Key Laboratory of Weak Light Nonlinear Photonics, Ministry of Education, Teda Applied Physics Institute and School of Physics, Nankai University, Tianjin 300457, China

³ Institute of Physics, Chinese Academy of Sciences, Beijing 100190, China

⁴ School of Physical Sciences, University of Chinese Academy of Sciences, Beijing 100190, China

⁵ Theoretical Quantum Physics Laboratory, RIKEN Cluster for Pioneering Research, Wako-shi, Saitama 351-0198, Japan

⁶ CAS Center for Excellence in Topological Quantum Computation, University of Chinese Academy of Sciences, Beijing 100190, China

⁷ School of Physics, Northwest University, Xi'an 710127, China

[†] These authors contributed equally;

^{*} To whom correspondence should be addressed;

E-mail: kaixu@iphy.ac.cn, liuzb@nankai.edu.cn, zhendongli@bnu.edu.cn, hfan@iphy.ac.cn

Contents

1	Variational quantum response (VQR) approach	30
1.1	Algorithm for linear response properties	30
1.2	Algorithms for the cross term $ \langle \Psi_0 \hat{V}^\dagger \hat{A}(\omega) x \rangle ^2$	34

2	Device information	38
2.1	Qubit information	38
2.2	Crosstalks	39
2.3	$\sqrt{i\text{SWAP}}$ gate	40
3	Two-qubit simulations for H_2 and polyacenes	45
3.1	Fermion-to-qubit mapping and wavefunction ansätze	45
3.2	Details of VQR algorithm	46
3.3	Error mitigation via spatial symmetry projection	48
3.4	VQE experiments	49
3.5	VQR experiments	52
3.6	Additional results from quantum chemistry calculations	53
3.6.1	Dipole polarizabilities of H_2 from FCI, HF, and DFT	53
3.6.2	Estimation of dynamic correlation by perturbation theory for polyacenes	54
4	Four-qubit simulations for CO	58
4.1	Fermion-to-qubit mapping and wavefunction ansatz	58
4.2	Details of VQR algorithm	59
4.3	Error mitigation via spin symmetry projection	61
4.4	VQR experiments	62

1 Variational quantum response (VQR) approach

1.1 Algorithm for linear response properties

To compute linear response properties of molecules such as the electronic absorption spectra, we adopted the Born-Oppenheimer approximation and neglected relativistic effects [1]. Consequently, the status of a molecule is described by the time-independent Schrödinger equation,

$$\hat{H}_0|\Psi\rangle = E|\Psi\rangle, \quad (5)$$

with the electronic Hamiltonian \hat{H}_0 being

$$\hat{H}_0 = \sum_{i=1}^N \hat{h}_i + \sum_{i<j}^N \frac{1}{r_{ij}} + E_{\text{NN}}, \quad \hat{h}_i = -\frac{1}{2}\nabla_i^2 + \sum_{A=1}^M -\frac{Z_A}{r_{iA}} \quad (6)$$

where $E_{\text{NN}} = \sum_{A<B}^M \frac{Z_A Z_B}{R_{AB}}$ is a constant for a fixed nuclei configuration $\{(Z_A, \vec{R}_A)\}_{A=1}^M$ with Z_A being the nuclear charge of the A -th nucleus. Given a set of orthonormal molecular spin-orbitals $\{\phi_p(x)\}_{p=1}^n$ with the composite coordinate $x \equiv (\vec{r}, \zeta)$ composed of position \vec{r} and spin $\zeta \in \{\alpha, \beta\}$, the second quantized form [2] of \hat{H}_0 reads

$$\hat{H}_0 = \sum_{pq} [p|h|q] a_p^\dagger a_q + \sum_{pqrs} \frac{1}{2} [ps|qr] a_p^\dagger a_q^\dagger a_r a_s + E_{\text{NN}}, \quad (7)$$

$$[p|h|q] = \int dx \phi_p^*(x) \hat{h} \phi_q(x), \quad (8)$$

$$[ps|qr] = \int dx_1 dx_2 \phi_p^*(x_1) \phi_s(x_1) r_{12}^{-1} \phi_q(x_2) \phi_r(x_2), \quad (9)$$

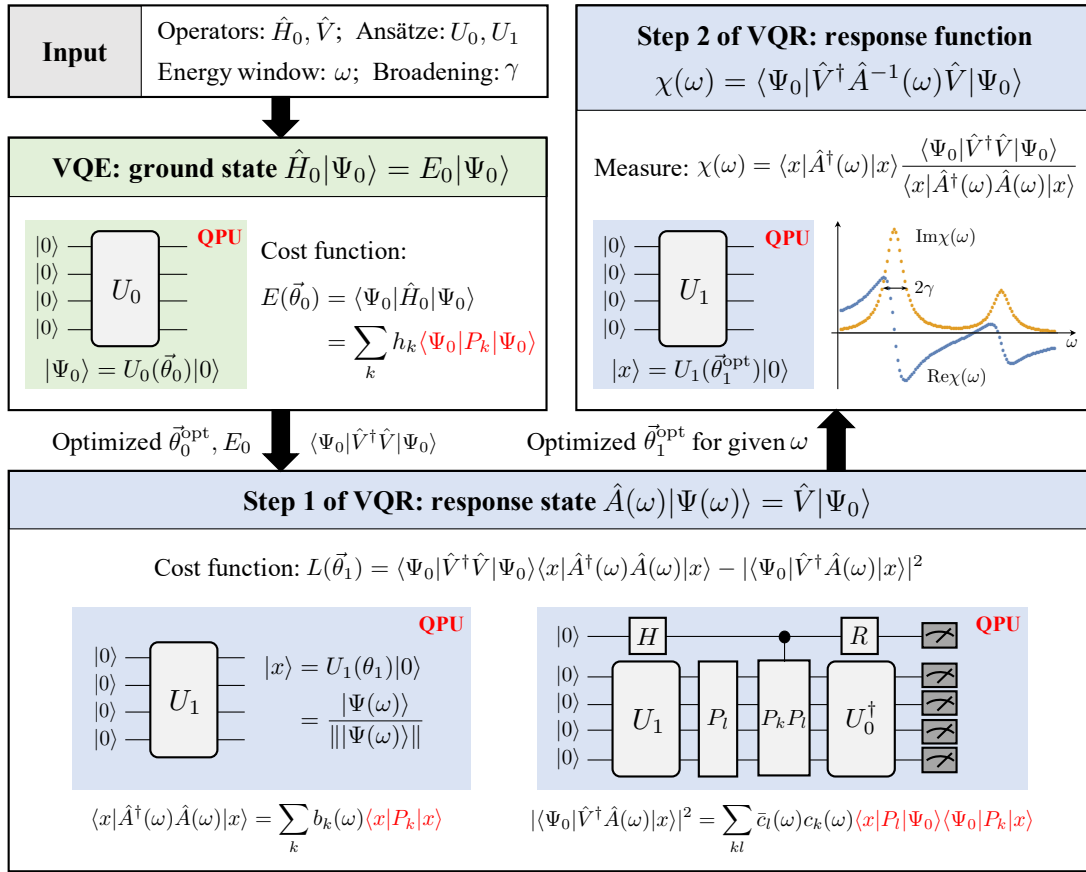
where a_p^\dagger (a_p) are fermionic creation (annihilation) operators. The coefficients $[p|h|q]$ and $[ps|qr]$ are the one-electron and two-electron molecular integrals in Mulliken notations, respectively, which can be computed from quantum chemistry packages. With a fermion-to-qubit mapping [3–5], \hat{H}_0 can be transformed to qubit operators,

$$\hat{H}_0 = \sum_k h_k P_k, \quad P_k = \sigma_0^k \otimes \sigma_1^k \otimes \cdots \otimes \sigma_{n-1}^k, \quad (10)$$

with $\sigma^k \in \{I, X, Y, Z\}$. Following from the two-body nature of electron-electron interaction (7), the number of Pauli terms (P_k) in \hat{H}_0 scales as $O(n^4)$. Similarly, a one-body perturbation operator \hat{V} such as the electric dipole operator can be expressed as

$$\hat{V} = \sum_k v_k P_k, \quad (11)$$

where the number of terms scales as $O(n^2)$.



Supplementary Figure 1: Variational hybrid quantum-classical algorithms for linear response properties of molecules. Terms highlighted in red are computed on quantum processor units (QPU).

The flowchart of variational hybrid quantum-classical algorithms for linear response properties of molecules is shown in Supplementary Fig. 1. The variational quantum eigensolver [6, 7]

(VQE) is first applied to compute the ground state, by optimizing the energy function of a variational ansatz $|\Psi_0\rangle = U(\vec{\theta}_0)|0\rangle$ with respect to the set of parameters $\vec{\theta}_0$,

$$E(\vec{\theta}_0) = \langle \Psi_0 | \hat{H}_0 | \Psi_0 \rangle = \sum_k h_k \langle \Psi_0 | P_k | \Psi_0 \rangle. \quad (12)$$

The expectation values $\langle \Psi_0 | P_k | \Psi_0 \rangle$ are measured on quantum computers.

The variational quantum response (VQR) approach for linear response properties of molecules includes two steps: obtaining the response state $|\Psi(\omega)\rangle$ at a given frequency in the interested regime and measuring the response function $\chi(\omega)$. The response state is determined from the linear response equation [8]

$$\hat{A}(\omega)|\Psi(\omega)\rangle = \hat{V}|\Psi_0\rangle, \quad \hat{A}(\omega) = \hat{H}_0 - E_0 - (\omega + i\gamma), \quad (13)$$

which can be solved by minimizing a cost function constructed using the Cauchy-Schwarz inequality,

$$L(\vec{\theta}_1) = \langle \Psi_0 | \hat{V}^\dagger \hat{V} | \Psi_0 \rangle \langle x | \hat{A}^\dagger(\omega) \hat{A}(\omega) | x \rangle - |\langle \Psi_0 | \hat{V}^\dagger \hat{A}(\omega) | x \rangle|^2, \quad (14)$$

with a variational ansatz for the normalized response state $|x\rangle = |\Psi(\omega)\rangle / \|\Psi(\omega)\rangle\| = U_1(\vec{\theta}_1)|0\rangle$. For brevity, we will omit the frequency dependence of the optimized set of parameters $\vec{\theta}_1$ and $|x\rangle$ in the following context. This cost function obeys $L(\vec{\theta}_1) \geq 0$, and the minimum is achieved for $|x\rangle \propto \hat{A}^{-1}(\omega) \hat{V} |\Psi_0\rangle$. Note that the choice of cost functions for solving linear systems of equations is not unique [9, 10]. For instance, another natural choice is $L(\vec{\theta}_1) = \|\hat{A}(\omega)|\Psi(\omega)\rangle - \hat{V}|\Psi_0\rangle\|^2$. In this work, we chose Eq. (14) due to the appearance of $|\langle \Psi_0 | \hat{V}^\dagger \hat{A}(\omega) | x \rangle|^2$, which enables a computation scheme with less controlled operations discussed in detail in the next subsection. Both $\langle \Psi_0 | \hat{V}^\dagger \hat{V} | \Psi_0 \rangle$ and $\langle x | \hat{A}^\dagger(\omega) \hat{A}(\omega) | x \rangle$ can be computed from measurements after preparing $|\Psi_0\rangle$ and $|x\rangle$, respectively. According to Eq. (13), $\hat{A}^\dagger(\omega) \hat{A}(\omega)$ can be written as

$$\hat{A}^\dagger(\omega) \hat{A}(\omega) = (\hat{H}_0 - E_0 - \omega)^2 + \gamma^2 = \sum_k b_k(\omega) P_k, \quad (15)$$

where the number of terms scales as $O(n^8)$. This scaling can be improved by using low-rank decompositions [11, 12].

After $|x\rangle$ is obtained at a given frequency, the response function $\chi(\omega)$ can be computed from [8]

$$\begin{aligned}
\chi(\omega) &= \langle \Psi_0 | \hat{V}^\dagger \hat{A}^{-1}(\omega) \hat{V} | \Psi_0 \rangle \\
&= \langle \Psi_0 | \hat{V}^\dagger (\hat{A}^\dagger(\omega))^{-1} \hat{A}^\dagger(\omega) \hat{A}^{-1}(\omega) \hat{V} | \Psi_0 \rangle \\
&= \langle \Psi(\omega) | \hat{A}^\dagger(\omega) | \Psi(\omega) \rangle \\
&= \langle x | \hat{A}^\dagger(\omega) | x \rangle \| |\Psi(\omega)\rangle \|^2.
\end{aligned} \tag{16}$$

Using Eq. (13), the square of the norm $\| |\Psi(\omega)\rangle \|^2$ is expressed as

$$\| |\Psi(\omega)\rangle \|^2 = \frac{\langle \Psi_0 | \hat{V}^\dagger \hat{V} | \Psi_0 \rangle}{\langle x | \hat{A}^\dagger(\omega) \hat{A}(\omega) | x \rangle}. \tag{17}$$

The final expression for computing $\chi(\omega)$ is

$$\chi(\omega) = \langle x | \hat{A}^\dagger(\omega) | x \rangle \frac{\langle \Psi_0 | \hat{V}^\dagger \hat{V} | \Psi_0 \rangle}{\langle x | \hat{A}^\dagger(\omega) \hat{A}(\omega) | x \rangle}, \tag{18}$$

which requires the measurements of $\langle x | \hat{A}^\dagger(\omega) | x \rangle$ and $\langle x | \hat{A}^\dagger(\omega) \hat{A}(\omega) | x \rangle$ given the optimized $|x\rangle$ at a given frequency. Eq. (18) can be written in a more revealing way by separating out the real and imaginary parts,

$$\text{Re}\chi(\omega) = \langle x | \hat{H}_0 - E_0 - \omega | x \rangle \| |\Psi(\omega)\rangle \|^2 = \langle x | \hat{H}_0 - E_0 - \omega | x \rangle \frac{\langle \Psi_0 | \hat{V}^\dagger \hat{V} | \Psi_0 \rangle}{\langle x | \hat{A}^\dagger(\omega) \hat{A}(\omega) | x \rangle}, \tag{19}$$

$$\text{Im}\chi(\omega) = \gamma \| |\Psi(\omega)\rangle \|^2 = \gamma \frac{\langle \Psi_0 | \hat{V}^\dagger \hat{V} | \Psi_0 \rangle}{\langle x | \hat{A}^\dagger(\omega) \hat{A}(\omega) | x \rangle}. \tag{20}$$

This shows that the peaks in $\text{Im}\chi(\omega)$, which is related with the absorption cross section, depend mainly on $1/\langle x | \hat{A}^\dagger(\omega) \hat{A}(\omega) | x \rangle$. To get a deeper understanding, we can find from Eq. (17) using the spectral decomposition for $|\Psi(\omega)\rangle$

$$\langle x | \hat{A}^\dagger(\omega) \hat{A}(\omega) | x \rangle = \frac{\langle \Psi_0 | \hat{V}^\dagger \hat{V} | \Psi_0 \rangle}{\| |\Psi(\omega)\rangle \|^2} = \frac{\langle \Psi_0 | \hat{V}^\dagger \hat{V} | \Psi_0 \rangle}{\sum_n \frac{|\langle \Psi_n | \hat{V} | \Psi_0 \rangle|^2}{(\omega_{n0} - \omega)^2 + \gamma^2}}, \tag{21}$$

such that

$$\text{Im}\chi(\omega) = \sum_n |\langle \Psi_n | \hat{V} | \Psi_0 \rangle|^2 \frac{\gamma}{(\omega_{n0} - \omega)^2 + \gamma^2}, \quad (22)$$

which shows that $\text{Im}\chi(\omega)$ is a weighted superposition of Lorentzians, which have peaks at $\omega = \omega_{n0} = E_n - E_0$ and a common full width at half maximum (FWHM) 2γ .

Linear response properties of molecules can be computed from the generic term $\chi(\omega)$ by choosing different \hat{V} . For instance, the zz -component of the dynamic polarizabilities can be written as

$$\begin{aligned} \alpha_{zz}(\omega) &= \sum_{n>0} \frac{\langle \Psi_0 | \hat{z} | \Psi_n \rangle \langle \Psi_n | \hat{z} | \Psi_0 \rangle}{\omega_{n0} - (\omega + i\gamma)} + \sum_{n>0} \frac{\langle \Psi_0 | \hat{z} | \Psi_n \rangle \langle \Psi_n | \hat{z} | \Psi_0 \rangle}{\omega_{n0} + (\omega + i\gamma)} \\ &= \chi(\omega) \Big|_{\hat{V} \rightarrow \hat{z}} + \chi(\omega) \Big|_{\hat{V} \rightarrow \hat{z}, \omega \rightarrow -\omega, \gamma \rightarrow -\gamma}. \end{aligned} \quad (23)$$

In this work, we only consider the first term which is the resonant contribution [13]. The second anti-resonant contribution is usually small and can be included using the same VQR approach if necessary. Other off-diagonal components can be computed by invoking the polarization identity [8]. Similarly, the single-particle Green's functions $G_{ij}(\omega) = \langle \Psi_0 | a_i \hat{A}^{-1}(\omega) a_j^\dagger | \Psi_0 \rangle$ can also be computed from $\chi(\omega)$ using the same algorithm, simply by setting \hat{V} as the fermionic creation/annihilation operators.

1.2 Algorithms for the cross term $|\langle \Psi_0 | \hat{V}^\dagger \hat{A}(\omega) | x \rangle|^2$

The cross term $|\langle \Psi_0 | \hat{V}^\dagger \hat{A}(\omega) | x \rangle|^2$ can be computed in different ways. Using Eqs. (10) and (11), $\hat{V}^\dagger \hat{A}(\omega)$ can be written as

$$\hat{V}^\dagger \hat{A}(\omega) = \sum_k c_k(\omega) P_k, \quad (24)$$

where the number of terms scales as $O(n^6)$. To reduce the number of terms, using the fact that $|\Psi_0\rangle$ is also an eigenfunction of $\hat{A}(\omega)$, we can rewrite $\langle \Psi_0 | \hat{V}^\dagger \hat{A}(\omega) | x \rangle$ as

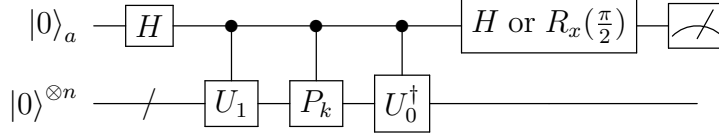
$$\langle \Psi_0 | \hat{V}^\dagger \hat{A}(\omega) | x \rangle = \langle \Psi_0 | [\hat{V}^\dagger, \hat{A}(\omega)] + \hat{A}(\omega) \hat{V}^\dagger | x \rangle = \langle \Psi_0 | [\hat{V}^\dagger, \hat{A}(\omega)] - (\omega + i\gamma) \hat{V}^\dagger | x \rangle. \quad (25)$$

The resulting effective operator $(\hat{V}^\dagger \hat{A}(\omega))_{\text{eff}} = [\hat{V}^\dagger, \hat{A}(\omega)] - (\omega + i\gamma)\hat{V}^\dagger$ is a two-body fermionic operator and the corresponding qubit operator will only contain $O(n^4)$ terms.

Given an appropriate expansion for $\hat{V}^\dagger \hat{A}(\omega)$ or its effective version, the most obvious way to compute $|\langle \Psi_0 | \hat{V}^\dagger \hat{A}(\omega) | x \rangle|^2$ is via the Hadamard test [9, 14]. With the following expansion,

$$\langle \Psi_0 | \hat{V}^\dagger \hat{A}(\omega) | x \rangle = \sum_k c_k(\omega) \langle 0 | U_0^\dagger P_k U_1 | 0 \rangle, \quad (26)$$

the expectation value of the unitary $U_0^\dagger P_k U_1$ can be computed with the following Hadamard test circuit



The disadvantage of this approach is that the large number of controlled unitaries is infeasible for realizations on near-term devices.

To avoid this deficiency, we propose a new strategy for computing the cross term, which can be viewed as trading controlled unitaries by measuring more circuits. The resulting circuits require less controlled Pauli operators than those presented in Ref. [10, 15]. The same method can also be applied to compute transition amplitudes between two states $|\langle \Psi_i | \hat{O} | \Psi_j \rangle|^2 = |\langle 0 | U_i^\dagger (\sum_k o_k P_k) U_j | 0 \rangle|^2$. To begin with, we divide the terms in the expansion

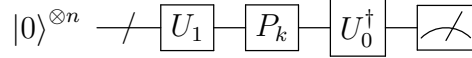
$$\begin{aligned} |\langle \Psi_0 | \hat{V}^\dagger \hat{A}(\omega) | x \rangle|^2 &= |\langle 0 | U_0^\dagger \left(\sum_k c_k(\omega) P_k \right) U_1 | 0 \rangle|^2 \\ &= \sum_{lk} \bar{c}_l(\omega) c_k(\omega) \langle 0 | U_1^\dagger P_l U_0 | 0 \rangle \langle 0 | U_0^\dagger P_k U_1 | 0 \rangle. \end{aligned} \quad (27)$$

into the diagonal ($l = k$) and off-diagonal ($l \neq k$) parts

$$\mathcal{E} = \sum_k |c_k(\omega)|^2 \langle 0|U_1^\dagger P_k U_0|0\rangle \langle 0|U_0^\dagger P_k U_1|0\rangle, \quad (28)$$

$$\begin{aligned} \mathcal{O} &= \sum_{l \neq k} \bar{c}_l(\omega) c_k(\omega) \langle 0|U_1^\dagger P_l U_0|0\rangle \langle 0|U_0^\dagger P_k U_1|0\rangle \\ &= 2 \sum_{l < k} [\text{Re}(\bar{c}_l(\omega) c_k(\omega)) \text{Re}(\langle 0|U_1^\dagger P_l U_0|0\rangle \langle 0|U_0^\dagger P_k U_1|0\rangle) \\ &\quad - \text{Im}(\bar{c}_l(\omega) c_k(\omega)) \text{Im}(\langle 0|U_1^\dagger P_l U_0|0\rangle \langle 0|U_0^\dagger P_k U_1|0\rangle)]. \end{aligned} \quad (29)$$

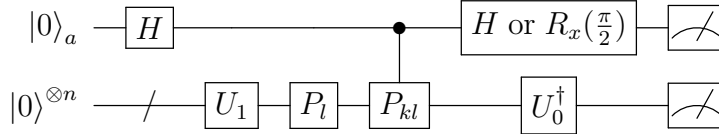
Then, each term in \mathcal{E} can be simply obtained using



$$\langle 0|U_1^\dagger P_k U_0|0\rangle \langle 0|U_0^\dagger P_k U_1|0\rangle = |\langle 0|U_0^\dagger P_k U_1|0\rangle|^2 = P_{0_0 \dots 0_{n-1}}, \quad (30)$$

where $P_{0_0 \dots 0_{n-1}}$ represents the probability of $|0_0 \dots 0_{n-1}\rangle$ observed for the prepared state $U_0^\dagger P_k U_1|0\rangle$.

For the off-diagonal terms, $\text{Re}(\langle 0|U_1^\dagger P_l U_0|0\rangle \langle 0|U_0^\dagger P_k U_1|0\rangle)$ and $\text{Im}(\langle 0|U_1^\dagger P_l U_0|0\rangle \langle 0|U_0^\dagger P_k U_1|0\rangle)$ can be computed via the following circuit



where $P_{kl} \equiv P_k P_l$ and H (or $R_x(\frac{\pi}{2})$) is used for the real (imaginary) part, viz.,

$$\begin{aligned} \text{Re}(\langle 0|U_1^\dagger P_l U_0|0\rangle \langle 0|U_0^\dagger P_k U_1|0\rangle) &= \frac{1}{4} (\langle x_l | (1 + P_{kl})^\dagger U_0 | 0 \rangle \langle 0 | U_0^\dagger (1 + P_{kl}) | x_l \rangle \\ &\quad - \langle x_l | (1 - P_{kl})^\dagger U_0 | 0 \rangle \langle 0 | U_0^\dagger (1 - P_{kl}) | x_l \rangle) \\ &= P_{0_0 0_1 \dots 0_n} - P_{1_0 0_1 \dots 0_n}, \end{aligned} \quad (31)$$

where $|x_l\rangle \equiv P_l U_1|0\rangle$. This scheme does not require controlled U_0 nor U_1 , but only controlled- P_{kl} , which is more feasible on near-term devices. In total, this general scheme requires $O(n^6)$ measurements for computing the cross term.

Further simplifications are possible for special cases. In this work, we utilize the facts that for our tests, the set of P_k can be simplified to single-qubit Pauli X operators X_k , as well as $\langle 0|U_0^\dagger U_1|0\rangle = 0$ and $\langle 0|U_0^\dagger X_k X_l U_1|0\rangle = 0$ due to spatial symmetry of the problems investigated. With these conditions, the real and imaginary parts of $\langle 0|U_1^\dagger X_l U_0|0\rangle \langle 0|U_0^\dagger X_k U_1|0\rangle$ ($k \neq l$) can be computed without using the ancilla qubit as follows:

(1) $\text{Re}(\langle 0|U_1^\dagger X_l U_0|0\rangle \langle 0|U_0^\dagger X_k U_1|0\rangle)$: By noting

$$\begin{aligned} |\langle 0|U_0^\dagger e^{-i\frac{\pi}{4}X_k} e^{-i\frac{\pi}{4}X_l} U_1|0\rangle|^2 &= \frac{1}{4} |\langle 0|U_0^\dagger (1 - i(X_k + X_l) - X_k X_l) U_1|0\rangle|^2 = \frac{1}{4} |\langle 0|U_0^\dagger (X_k + X_l) U_1|0\rangle|^2 \\ &= \frac{1}{4} (|\langle 0|U_0^\dagger X_k U_1|0\rangle|^2 + |\langle 0|U_0^\dagger X_l U_1|0\rangle|^2) + \frac{1}{2} \text{Re}(\langle 0|U_1^\dagger X_l U_0|0\rangle \langle 0|U_0^\dagger X_k U_1|0\rangle) \end{aligned} \quad (32)$$

the real part becomes

$$\text{Re}(\langle 0|U_1^\dagger X_l U_0|0\rangle \langle 0|U_0^\dagger X_k U_1|0\rangle) = 2|\langle 0|U_0^\dagger e^{-i\frac{\pi}{4}X_k} e^{-i\frac{\pi}{4}X_l} U_1|0\rangle|^2 - \frac{1}{2} \left(|\langle 0|U_0^\dagger X_k U_1|0\rangle|^2 + |\langle 0|U_0^\dagger X_l U_1|0\rangle|^2 \right), \quad (33)$$

where the first term can be computed by preparing the state $U_0^\dagger R_{x,k}(\frac{\pi}{2}) R_{x,l}(\frac{\pi}{2}) U_1|0\rangle$.

(2) $\text{Im}(\langle 0|U_1^\dagger X_l U_0|0\rangle \langle 0|U_0^\dagger X_k U_1|0\rangle)$: By using

$$|\langle 0|U_0^\dagger (X_l + iX_k) U_1|0\rangle|^2 = |\langle 0|U_0^\dagger X_l (1 + iX_l X_k) U_1|0\rangle|^2 = 2|\langle 0|U_0^\dagger X_l e^{i\frac{\pi}{4}X_l X_k} U_1|0\rangle|^2, \quad (34)$$

the imaginary part becomes

$$\text{Im}(\langle 0|U_1^\dagger X_l U_0|0\rangle \langle 0|U_0^\dagger X_k U_1|0\rangle) = -|\langle 0|U_0^\dagger X_l e^{i\frac{\pi}{4}X_l X_k} U_1|0\rangle|^2 + \frac{1}{2} \left(|\langle 0|U_0^\dagger X_l U_1|0\rangle|^2 + |\langle 0|U_0^\dagger X_k U_1|0\rangle|^2 \right), \quad (35)$$

where the first term can be computed by preparing the state $U_0^\dagger X_l e^{i\frac{\pi}{4}X_l X_k} U_1|0\rangle$.

In summary, we have derived a general scheme using Eq. (31) for evaluating the cross term in the cost function. In addition, the ancilla qubit can be removed for special cases. Eqs. (33) and (35) are the actual expressions used for systems investigated in the present work.

2 Device information

2.1 Qubit information

The superconducting quantum processor used in our experiment consists of 20 transmon qubits, which are interconnected by a central bus resonator with frequency fixed at around $\omega_R/2\pi \approx 5.51$ GHz, as shown in Fig. 2a in the main text. The detailed fabrication processes and basic circuit elements can be found in Ref. [16]. Five qubits, denoted by Q_3 , Q_6 , Q_{13} , Q_{14} , Q_{20} , are used in this work, where Q_{14} and Q_{20} are used in the experiments for H_2 and polyacenes, while Q_3 , Q_6 , Q_{13} , and Q_{20} are employed for studying the CO molecule. Their resonant frequencies, denoted by $\omega_{\text{idle}}/2\pi$, are carefully arranged to minimize any possible unwanted interaction and crosstalk error among qubits during single-qubit operations. All relevant information about the employed qubits are summarized in Supplementary Table 1. The anharmonicity of the six qubits are about 245 MHz. The measured qubit characteristic decoherence parameters (energy relaxation time T_1 and Ramsey Gaussian dephasing time T_2^*) can be found in Supplementary Table 1, which are far greater than the circuit length (several hundred nanoseconds). Single qubit operations, including the $X/2$ ($=R_x(\pi/2)$) and X ($=R_x(\pi)$) gates, have a timescale length of 30 ns and a FWHM of 15 ns, respectively. The quadrature correction term with DRAG coefficient α are optimized following the DRAG theory to minimize the leakage to higher energy levels [17]. The readout pulses for all qubits are 1.5 μs in length, and the readout powers and frequencies are optimized for a high-visibility and low-state-error readout. As shown in Supplementary Table 1, the readout fidelities, denoted by F_0 and F_1 , are no less than 0.981 and 0.918 for $|0\rangle$ and $|1\rangle$ state, respectively. During the experiment, we periodically calibrate the amplitude of DC source output for the idle frequency and the pulse amplitude of single-qubit gates of each qubit to avoid the performance drifts with time. We also monitor the readout fidelities in Supplementary Fig. 2 during the experiment in order to perform the real-time correction of readout

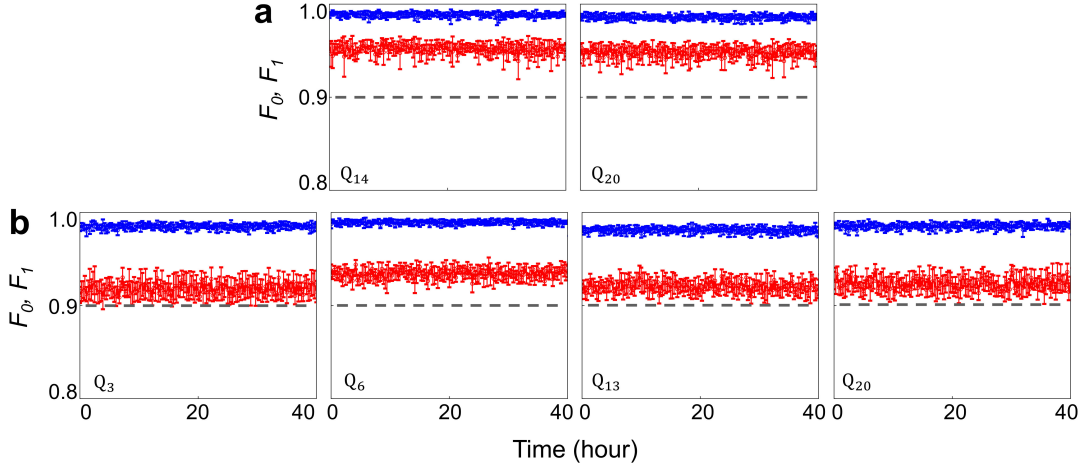
errors [18], by applying the inverse of the tensor product of matrices $\begin{pmatrix} F_0 & 1 - F_1 \\ 1 - F_0 & F_1 \end{pmatrix}$ for the involved qubits to the measured occupation probabilities.

Supplementary Table 1: Qubit characteristics. ω_{idle} is the idle frequency of qubit where decoherence parameters (including energy relaxation time T_1 and Ramsey Gaussian dephasing time T_2^*) are measured. F_0 (F_1) is the measurement probability of $|0\rangle$ ($|1\rangle$) when the qubit is prepared in $|0\rangle$ ($|1\rangle$), which is used to mitigate the readout errors.

	H ₂ and polyacenes		CO			
	Q ₁₄	Q ₂₀	Q ₃	Q ₆	Q ₁₃	Q ₂₀
$\omega_{\text{idle}}/2\pi$ (GHz)	5.200	5.260	5.190	5.130	5.080	5.025
T_1 (μ s)	23.4	33.9	16.1	28.8	15.5	22.9
T_2^* (μ s)	3.7	3.6	2.5	3.5	2.2	2.4
F_0	0.989	0.986	0.985	0.989	0.981	0.986
F_1	0.952	0.948	0.918	0.934	0.920	0.922

2.2 Crosstalks

The Z line crosstalks between different qubit pairs are calibrated based on the Z-crosstalk matrix \widetilde{M}_Z as done in Ref. [19], where each element denotes the zpa (Z pulse amplitude) sensed by Q_j when a unitary zpa is applied to Q_i . Note that all $(\widetilde{M}_Z)_{i,j}$ elements are less than 2.5%, as shown in Supplementary Fig. 3a. All zpa applied to qubits are calibrated based on the mapping relationship $\widetilde{Z}_{\text{sensed}} = \widetilde{M}_Z \cdot \widetilde{Z}_{\text{applied}}$, where $\widetilde{Z}_{\text{sensed}}$ and $\widetilde{Z}_{\text{applied}}$ represent the zpa sensed and applied to qubits, respectively. We also characterize the XY line crosstalks by measuring the occupation probabilities of Q_j when Q_i is prepared in $|0\rangle$ and $|1\rangle$, respectively. The crosstalks between XY lines are caused by insufficient crossover bonding or the frequency leakage, while the latter can be efficiently ameliorated by calibrating the room temperature electronics and carefully arranging the idle frequency of qubits. The XY-crosstalk matrix \widetilde{M}_{XY} are shown in Supplementary Fig. 3b, and all $(\widetilde{M}_{XY})_{i,j}$ elements do not exceed 0.8%, indicating the feasibility for stimulating all qubits simultaneously.



Supplementary Figure 2: The readout fidelities of the used qubits with error bars monitored over 40 hours. The results corresponding to $|0\rangle$ and $|1\rangle$ state are denoted by F_0 (blue) and F_1 (red), respectively. a, Qubits used in experiments for H_2 and polyacenes. b, Qubits used in experiments for CO.

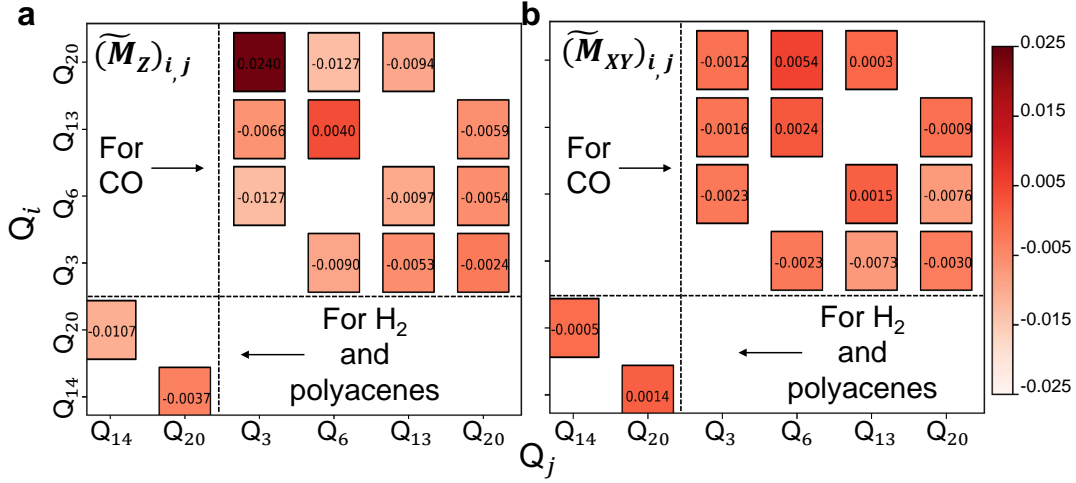
2.3 \sqrt{i} SWAP gate

In our experiment, the two-qubit entangling gate \sqrt{i} SWAP, with the matrix form

$$\sqrt{i}\text{SWAP} = \begin{pmatrix} 1 & 0 & 0 & 0 \\ 0 & \frac{\sqrt{2}}{2} & \frac{\sqrt{2}}{2}i & 0 \\ 0 & \frac{\sqrt{2}}{2}i & \frac{\sqrt{2}}{2} & 0 \\ 0 & 0 & 0 & 1 \end{pmatrix}, \quad (36)$$

is generated by tuning all the involved qubits on-resonance with a certain characteristic interaction time $t_{\sqrt{i}\text{SWAP}} = \frac{\pi}{4|\lambda|}$, where λ is negative and approximately equals to \tilde{g}^2/Δ , \tilde{g} is defined as the average coupling strength between qubit and central bus resonator, and Δ denotes the detuning between the on-resonance frequency and bus resonator frequency. Here, $t_{\sqrt{i}\text{SWAP}}$ is optimized to be 43.8 ns, 43.5 ns, 48.1 ns and 56.6 ns for different pairs of qubits Q_{14} - Q_{20} , Q_3 - Q_6 , Q_3 - Q_{13} , and Q_6 - Q_{20} , respectively, see Supplementary Table 2.

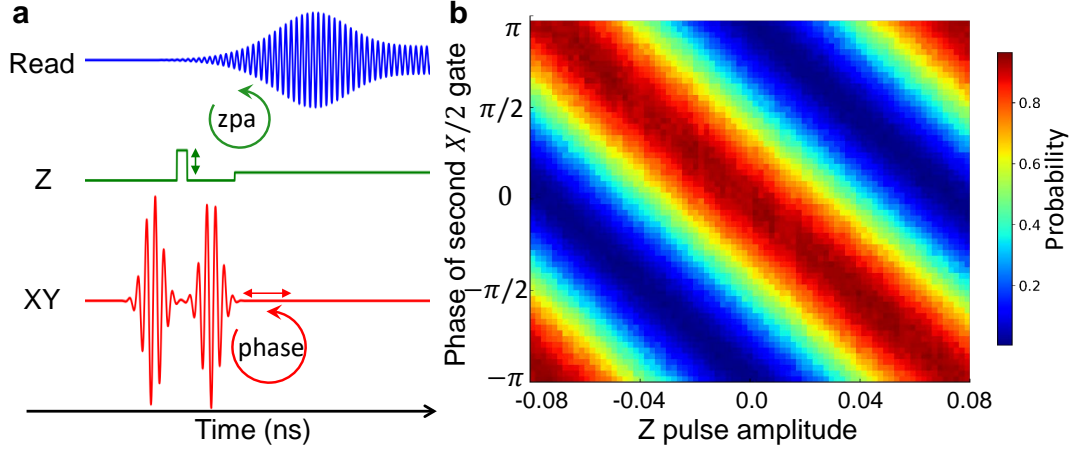
To cancel out the dynamical phases accumulated during the entangling interaction, single-qubit phase gates are employed [20], which are optimized by numerical calculations and then



Supplementary Figure 3: Z- and XY-crosstalk matrices \widetilde{M}_Z and \widetilde{M}_{XY} . a, Z-crosstalk matrix \widetilde{M}_Z , where each element $(\widetilde{M}_Z)_{i,j}$ denotes the needed zpa of Q_j when a unitary zpa is applied to Q_i . b, XY-crosstalk matrix \widetilde{M}_{XY} , where each element $(\widetilde{M}_{XY})_{i,j}$ represents the difference of measured occupation probabilities of Q_j when Q_i is stimulated to $|1\rangle$ with a X gate.

added on each qubit before and after the interaction process. The front phase gates guarantee that the x axes of the Bloch spheres for all qubits are aligned at the beginning of the interaction in the rotating frame of the on-resonance frequency, while the latter ones are to make sure that x axis of each qubit is aligned in the rotating frame of its idle frequency at the end of the interaction. All phase gates are realized by amplitude-adjustable Z square pulses with a width of 20 ns, indicating a frequency shift of 25 MHz corresponding to the idle point for the phase accumulation of π . We can easily map the relationship between Z pulse amplitude and phase by inserting an amplitude-tunable Z square pulses between two $X/2$ gates and change the microwave phase of the last $X/2$ gate, as shown in Supplementary Fig. 4.

To characterize the performance of \sqrt{i} SWAP gates, quantum process tomography [21, 22] (QPT) is performed by preparing a full set of 6^n input states $\bigotimes_j^n \{I, \pm X/2, \pm Y/2, X\}$ (n denotes the number of qubits, and $n = 2$ here). We compare the ideal and experimental process matrices [23] χ_{ideal} and χ_{exp} , and calculate the gate fidelities $F = \text{tr}(\chi_{\text{exp}}\chi_{\text{ideal}})$. The interac-

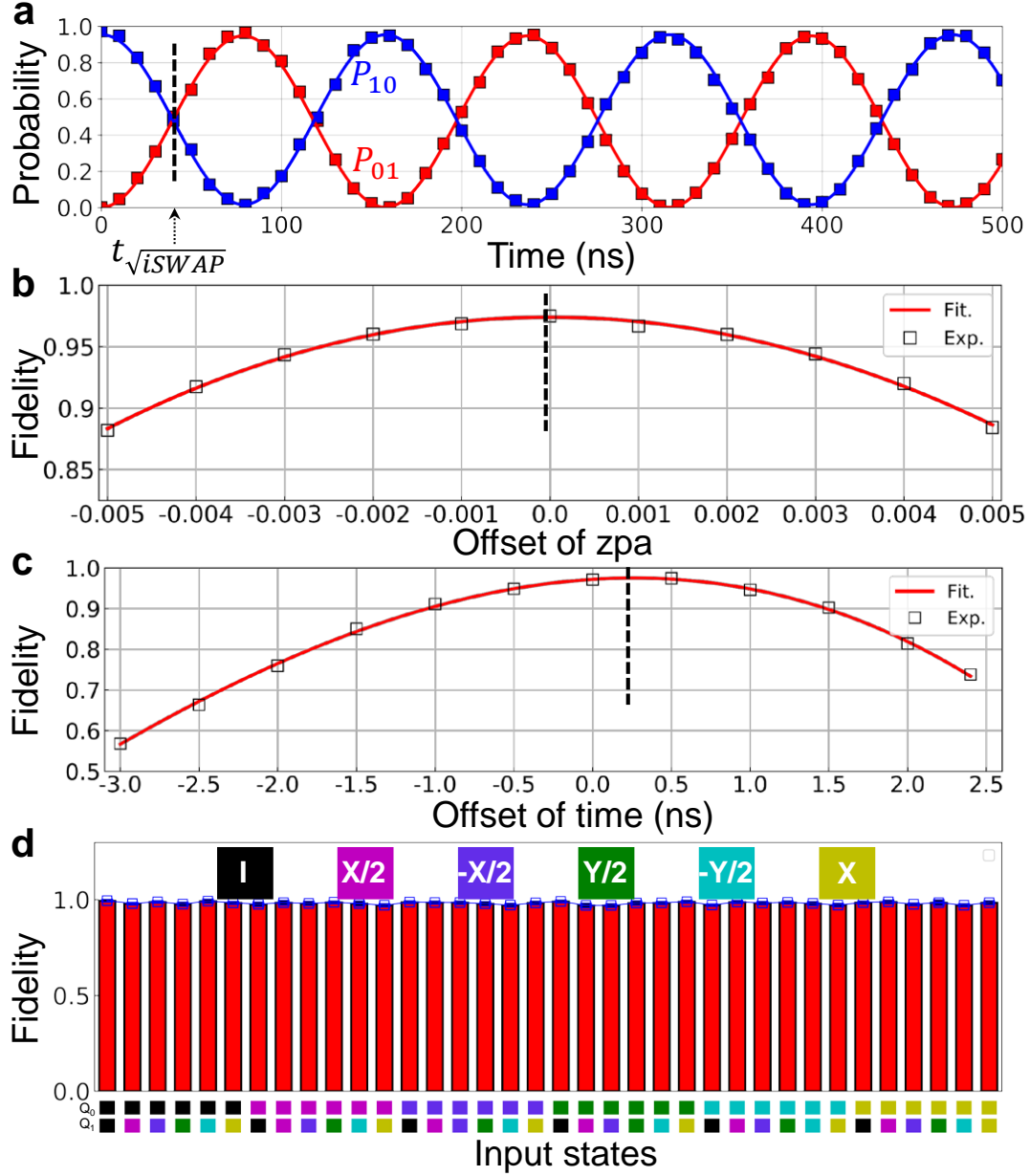


Supplementary Figure 4: Generation of single-qubit phase gate. a, Pulse sequence for getting the relationship between Z pulse amplitude and phase. b, The measured probability of $|1\rangle$ state with the change of Z pulse amplitude (zpa) and microwave phase of the second $X/2$ gate.

tion frequencies $\omega_I/2\pi$ and fidelities characterized by QPT for different qubit pairs (Q_{14} - Q_{20} , Q_3 - Q_6 , Q_3 - Q_{13} , and Q_6 - Q_{20}) involved in our experiments are summarized in Supplementary Table 2. We have optimized some important parameters of the \sqrt{i} SWAP gate by QPT strategy, e.g. the characteristic gate time $t_{\sqrt{i}\text{SWAP}}$ and zpa for tuning qubits on-resonance with each other. Take the gate Q_{14} - Q_{20} for an instance, we firstly estimate $t_{\sqrt{i}\text{SWAP}}$ and zpa through the superexchange (SE) [24] interaction mediated by the central bus resonator at the idle frequency of Q_{14} (detuned from the bus resonator frequency by 310 MHz), as the probability evolutions show in Supplementary Fig. 5a. Then, we perform QPT measurement dependent on the offset of $t_{\sqrt{i}\text{SWAP}}$ and zpa of Q_{20} , with the calculated fidelities plotted in Supplementary Fig. 5b and c, respectively. Fidelities of all 36 characteristic input states with error bars after optimization are shown in Supplementary Fig. 5d, yielding a gate fidelity over 0.98.

Supplementary Table 2: Characteristics of two-qubit $\sqrt{\text{iSWAP}}$ gates. Working points (ω_I), characteristic gate times ($t_{\sqrt{\text{iSWAP}}}$) and gate fidelities (F) estimated by quantum process tomography (QPT) for the four two-qubit gates used in our experiments.

	H ₂ and polyacenes		CO	
	Q ₁₄ -Q ₂₀	Q ₃ -Q ₆	Q ₃ -Q ₁₃	Q ₆ -Q ₂₀
$\omega_I/2\pi$ (GHz)	5.160	5.190	5.170	5.130
$t_{\sqrt{\text{iSWAP}}}$ (ns)	43.8	43.5	48.1	56.6
F	0.9806 \pm 0.0012	0.9766 \pm 0.0005	0.9679 \pm 0.0061	0.9508 \pm 0.0050



Supplementary Figure 5: Optimization of the $\sqrt{i}\text{SWAP}$ gate by QPT. a, Superexchange interaction for $Q_{14}\text{-}Q_{20}$. A characteristic gate time $t_{\sqrt{i}\text{SWAP}}$ can be identified by the time-modulated probabilities P_{10} (blue squares) and P_{01} (red squares) for state $|10\rangle$ and $|01\rangle$, respectively. b,c, Gate fidelity with the change of zpa and interaction time $t_{\sqrt{i}\text{SWAP}}$. The blank squares are experimental results and the red lines are fitted data. d, The calculated fidelities for 36 input states $\bigotimes_{j=1}^{n=2} \{I, \pm X/2, \pm Y/2, X\}$.

3 Two-qubit simulations for H₂ and polyacenes

3.1 Fermion-to-qubit mapping and wavefunction ansätze

The two-qubit simulations are carried out for H₂ in the STO-3G basis and polyacenes within a two-electron-in-two-orbital active space model including the highest occupied molecular orbital (HOMO) and the lowest unoccupied molecular orbital (LUMO). The prototypical molecule H₂ is investigated at three bond distances, R_e , $2R_e$, and $3R_e$, where $R_e = 0.74144$ Å is the experimental equilibrium bond distance [25]. Geometries of polyacenes are optimized at the density functional theory (DFT) level of theory using the B3LYP [26,27] hybrid functional and the 6-31G* basis set. For these two kinds of systems, the molecular orbitals obtained from spin-restricted Hartree-Fock (RHF) calculations are taken as the one-electron orbital basis for quantum simulations based on second quantization.

Consider H₂ as example, the Bravyi-Kitaev (BK) transformation [4,5] leads to the following mapping of occupation number vectors (ONVs),

$$\begin{aligned} |n_0 n_1 n_2 n_3\rangle &= |n_g n_u n_{\bar{g}} n_{\bar{u}}\rangle \\ \rightarrow |n_g(n_u + n_g \bmod 2) n_{\bar{g}}(n_{\bar{u}} + n_{\bar{g}} + n_u + n_g \bmod 2)\rangle &= |n_g p_e^\alpha n_{\bar{g}} p_e\rangle. \end{aligned} \quad (37)$$

where $n \in \{0, 1\}$ denotes the occupation of an molecular spin-orbital (MO), g (u) refers to the MO with gerade (ungerade) symmetry due to the existence of inversion symmetry in H₂, p_e (p_e^α) represents the parity of the number of total (alpha) electrons N_e (N_e^α). For particle number and spin projection conserving Hamiltonian, we can restrict the space of interest to the subspace with well-defined p_e and p_e^α . This is referred as the Z_2 reduction [28], which enables the removal of two qubits. The final ONV of qubits after the Z_2 reduction becomes

$$|q_0 q_1\rangle = |n_g n_{\bar{g}}\rangle, \quad (38)$$

which implies the following mapping of determinants with $N_e = 2$ and $N_e^\alpha = 1$ to ONVs of

qubits

$$\begin{aligned}
|g\bar{g}\rangle &\rightarrow |11\rangle, \\
|u\bar{u}\rangle &\rightarrow |00\rangle, \\
|g\bar{u}\rangle &\rightarrow |10\rangle, \\
|u\bar{g}\rangle &\rightarrow |01\rangle.
\end{aligned} \tag{39}$$

The same mapping works for polyacenes within the active space model, except that the labels g and u will interchange for HOMO and LUMO, depending on the number of rings, see Fig. 4 in the main text.

The ground state is in the subspace $V_g = \{|g\bar{g}\rangle, |u\bar{u}\rangle\} = \{|11\rangle, |00\rangle\}$, while the response state for the dipole perturbation $\hat{V} = \hat{z}$ resides in the subspace $V_u = \{|g\bar{u}\rangle, |u\bar{g}\rangle\} = \{|10\rangle, |01\rangle\}$. The wavefunction ansatz shown in Fig. 3a in the main text gives a parameterization

$$|\Psi(\theta_0)\rangle = U_0(\theta_0)|0\rangle = |11\rangle \cos(\theta_0/2) + |00\rangle \sin(\theta_0/2), \tag{40}$$

up to an irrelevant global phase. The ansatz for $|x(\theta_1)\rangle$ in Fig. 3c for the dipole perturbation $\hat{V} = \hat{z}$ gives

$$|x(\theta_1)\rangle = U_1(\theta_1)|0\rangle = X_1 U_0(\theta_1)|0\rangle = |10\rangle \cos(\theta_1/2) + |01\rangle \sin(\theta_1/2), \tag{41}$$

up to a global phase. These are exact parameterizations for the ground and response states. In particular, the exact response state can always be found at $\theta_1 = \pi/2$ due to spin symmetry, as $|x(\theta_1 = \pi/2)\rangle = \frac{1}{\sqrt{2}}(|10\rangle + |01\rangle)$ corresponds to the singlet excited state due to the singe excitation from g to u .

3.2 Details of VQR algorithm

The Hamiltonian \hat{H}_0 after the BK mapping with the Z_2 reduction reads

$$\hat{H}_0 = h_0 I + h_1 Z_0 + h_2 Z_1 + h_3 Z_0 Z_1 + h_4 X_0 X_1. \tag{42}$$

For the dipole perturbation $\hat{V} = \hat{z} = z_{ug}(a_u^\dagger a_g + a_{\bar{u}}^\dagger a_{\bar{g}}) + \text{h.c.}$ with $z_{ug} = \langle u | \hat{z} | g \rangle$, the corresponding qubit operator after the BK transformation and the Z_2 reduction becomes

$$\hat{V} = v_0(X_0 + X_1), \quad v_0 = z_{ug}, \quad (43)$$

The coefficients h_k and v_0 for different systems are summarized in Supplementary Table 3.

Supplementary Table 3: Coefficients (in atomic unit) of Pauli operators in \hat{H}_0 (42) and \hat{V} (43) for H_2 at different bond distances $R = sR_e$ ($s = 1, 2, 3$) and polyacenes with different number of rings ($n = 2, 3, 4, 5$).

	H_2			polyacenes			
	$s = 1$	$s = 2$	$s = 3$	$n = 2$	$n = 3$	$n = 4$	$n = 5$
$h_0 (h_{II})$	-1.053716	-1.012393	-0.895897	-0.611117	-0.558265	-0.524089	-0.499055
$h_1 (h_{ZI})$	0.393959	0.132405	0.042584	0.098308	0.077231	0.062505	0.051971
$h_2 (h_{IZ})$	0.393959	0.132405	0.042584	0.098308	0.077231	0.062505	0.051971
$h_3 (h_{ZZ})$	0.011236	0.004326	0.000815	0.001972	0.001323	-0.000958	0.000731
$h_4 (h_{XX})$	0.181291	0.228430	0.270319	0.044417	0.037979	0.034403	0.032027
v_0	-0.931343	-1.452302	-2.108703	1.444951	1.510664	1.593675	1.680618

With Eqs. (42) and (43), the following expansions can be found

$$\hat{V}^\dagger \hat{V} = w_0 I + w_1 X_0 X_1, \quad (44)$$

$$\hat{A}(\omega) = h'_0(\omega) I + h_1 Z_0 + h_2 Z_1 + h_3 Z_0 Z_1 + h_4 X_0 X_1, \quad (45)$$

$$\hat{A}^\dagger(\omega) \hat{A}(\omega) = b_0(\omega) I + b_1(\omega) Z_0 + b_2(\omega) Z_1 + b_3(\omega) Z_0 Z_1 + b_4(\omega) X_0 X_1 + b_5(\omega) Y_0 Y_1, \quad (46)$$

$$\begin{aligned} \hat{V}^\dagger \hat{A}(\omega) = & v_0 [h'_0(\omega) X_0 + h_1(-iY_0) + h_2 X_0 Z_1 + h_3(-iY_0) Z_1 + h_4 X_1] \\ & + [h'_0(\omega) X_1 + h_1 X_1 Z_0 + h_2(-iY_1) + h_3 Z_0(-iY_1) + h_4 X_0], \end{aligned} \quad (47)$$

where $h'_0(\omega) = h_0 - E_0 - (\omega + i\gamma)$. For $\langle \Psi_0 | \hat{V}^\dagger \hat{A}(\omega) | x \rangle$, where $|\Psi_0\rangle \in V_g$ and $|x\rangle \in V_u$, an effective operator $(\hat{V}^\dagger \hat{A}(\omega))_{\text{eff}}$, which leads to the same matrix element, can be obtained from $\hat{V}^\dagger \hat{A}(\omega)$ by the replacements $X_i Z_j \rightarrow iY_i$ and $Y_i Z_j \rightarrow -iX_i$ ($i \neq j$). Together with the condition $h_1 = h_2$, this leads to

$$(\hat{V}^\dagger \hat{A}(\omega))_{\text{eff}} = v_0 [h'_0(\omega) - h_3 + h_4] (X_0 + X_1) \equiv c_0(\omega) (X_0 + X_1). \quad (48)$$

The coefficients of Pauli operators in $\hat{A}^\dagger(\omega)\hat{A}(\omega)$ and $(\hat{V}^\dagger\hat{A}(\omega))_{\text{eff}}$ are summarized in Supplementary Table 4.

Using Eqs. (48) and (33), the cross term (27) can be expressed as

$$\begin{aligned}
|\langle\Psi_0|\hat{V}^\dagger\hat{A}(\omega)|x\rangle|^2 &= |c_0(\omega)|^2|\langle\Psi_0|(X_0 + X_1)|x\rangle|^2 \\
&= |c_0(\omega)|^2(|\langle\Psi_0|X_0|x\rangle|^2 + |\langle\Psi_0|X_1|x\rangle|^2 + 2\text{Re}(\langle\Psi_0|X_0|x\rangle\langle x|X_1|\Psi_0\rangle)) \\
&= 4|c_0(\omega)|^2|\langle 0|U_0^\dagger R_{x,0}(\frac{\pi}{2})R_{x,1}(\frac{\pi}{2})U_1|0\rangle|^2.
\end{aligned} \tag{49}$$

This simple expression only requires the quantum circuit shown in Fig. 3b in the main text to construct the cross term.

Supplementary Table 4: Expressions for the coefficients of Pauli operators in $\hat{A}^\dagger(\omega)\hat{A}(\omega)$ (46) and $(\hat{V}^\dagger\hat{A}(\omega))_{\text{eff}}$ (48) for the two-qubit problem.

	expressions
$b_0(\omega) (b_{II}(\omega))$	$\gamma^2 + (h_{II} - E_0 - \omega)^2 + h_{IZ}^2 + h_{ZI}^2 + h_{ZZ}^2 + h_{XX}^2$
$b_1(\omega) (b_{ZI}(\omega))$	$2[h_{ZI}(h_{II} - E_0 - \omega) + h_{IZ}h_{ZZ}]$
$b_2(\omega) (b_{IZ}(\omega))$	$2[h_{IZ}(h_{II} - E_0 - \omega) + h_{ZI}h_{ZZ}]$
$b_3(\omega) (b_{ZZ}(\omega))$	$2[h_{ZZ}(h_{II} - E_0 - \omega) + h_{IZ}h_{ZI}]$
$b_4(\omega) (b_{XX}(\omega))$	$2h_{XX}(h_{II} - E_0 - \omega)$
$b_5(\omega) (b_{YY}(\omega))$	$-2h_{XX}h_{ZZ}$
$c_0(\omega)$	$v_0[h_{II} - h_{ZZ} + h_{XX} - E_0 - (\omega + i\gamma)]$

3.3 Error mitigation via spatial symmetry projection

For the subspaces V_g and V_u , the symmetry projectors can be found as

$$\mathcal{P}_g = |00\rangle\langle 00| + |11\rangle\langle 11| = \frac{1}{4}[(I_1 + Z_1)(I_0 + Z_0) + (I_1 - Z_1)(I_0 - Z_0)] = \frac{1}{2}(I + Z_0Z_1), \tag{50}$$

$$\mathcal{P}_u = |01\rangle\langle 01| + |10\rangle\langle 10| = \frac{1}{4}[(I_1 + Z_1)(I_0 - Z_0) + (I_1 - Z_1)(I_0 + Z_0)] = \frac{1}{2}(I - Z_0Z_1). \tag{51}$$

For the ground state, instead of computing E_0 from $|\Psi_0\rangle$ via

$$E_0^{\text{raw}} = \langle\Psi_0|\hat{H}_0|\Psi_0\rangle = h_{II} + h_{IZ}(\langle I_1Z_0\rangle + \langle Z_1I_0\rangle) + h_{ZZ}\langle Z_1Z_0\rangle + h_{XX}\langle X_1X_0\rangle + h_{YY}\langle Y_1Y_0\rangle, \tag{52}$$

an improved error-mitigated (EM) estimator with the symmetry-projected state $|\tilde{\Psi}_0\rangle = \frac{\mathcal{P}_g|\Psi_0\rangle}{\sqrt{\langle\Psi_0|\mathcal{P}_g|\Psi_0\rangle}}$ can be derived using

$$\hat{H}_0 Z_1 Z_0 = h_{II} Z_1 Z_0 + h_{IZ}(Z_1 I_0 + I_1 Z_0) + h_{ZZ} I_1 I_0 - h_{XX} Y_1 Y_0 - h_{YY} X_1 X_0, \quad (53)$$

such that

$$\begin{aligned} E_0^{\text{EM}} &= \langle\tilde{\Psi}_0|\hat{H}_0|\tilde{\Psi}_0\rangle = \frac{\langle\Psi_0|\hat{H}_0\mathcal{P}_g|\Psi_0\rangle}{\langle\Psi_0|\mathcal{P}_g|\Psi_0\rangle} \\ &= (h_{II} + h_{ZZ}) + \frac{2h_{IZ}(\langle I_1 Z_0\rangle + \langle Z_1 I_0\rangle) + (h_{XX} - h_{YY})(\langle X_1 X_0\rangle - \langle Y_1 Y_0\rangle)}{1 + \langle Z_1 Z_0\rangle} \end{aligned} \quad (54)$$

using the commutativity property $[\mathcal{P}_g, \hat{H}_0] = 0$. The same strategy can be applied to estimate $\langle\Psi_0|\hat{V}^\dagger\hat{V}|\Psi_0\rangle$ (44).

For $\langle x|\hat{A}^\dagger(\omega)\hat{A}(\omega)|x\rangle$ and $\langle x|\hat{A}^\dagger(\omega)|x\rangle$ required in the VQR calculations, \mathcal{P}_u (51) can be used in a similar way. Consider the quantity $\langle x|\hat{A}^\dagger(\omega)\hat{A}(\omega)|x\rangle$ as example, which is crucial for computing the imaginary part of $\chi(\omega)$ (20),

$$\langle x|\hat{A}^\dagger(\omega)\hat{A}(\omega)|x\rangle^{\text{raw}} = b_{II} + b_{IZ}(\langle I_1 Z_0\rangle + \langle Z_1 I_0\rangle) + b_{ZZ}\langle Z_1 Z_0\rangle + b_{XX}\langle X_1 X_0\rangle + b_{YY}\langle Y_1 Y_0\rangle. \quad (55)$$

The error mitigated estimator with \mathcal{P}_u is

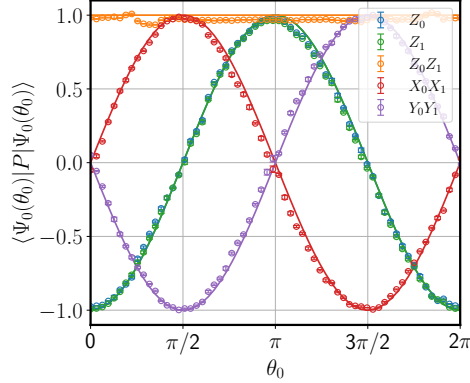
$$\langle x|\hat{A}^\dagger(\omega)\hat{A}(\omega)|x\rangle^{\text{EM}} = \frac{\langle x|\hat{A}^\dagger(\omega)\hat{A}(\omega)\mathcal{P}_u|x\rangle}{\langle x|\mathcal{P}_u|x\rangle} = (b_{II} - b_{ZZ}) + \frac{(b_{XX} + b_{YY})(\langle X_1 X_0\rangle + \langle Y_1 Y_0\rangle)}{1 - \langle Z_1 Z_0\rangle}. \quad (56)$$

In our experiments, to improve the accuracy this expression is used in both estimating $\langle x|\hat{A}^\dagger(\omega)\hat{A}(\omega)|x\rangle$ in the cost function $L(\theta_1)$ (14) as well as estimating $\langle x|\hat{A}^\dagger(\omega)\hat{A}(\omega)|x\rangle$ and $\langle x|\hat{A}^\dagger(\omega)|x\rangle$ for $\chi(\omega)$ (18).

3.4 VQE experiments

To find the ground state, we perform VQE experiments by scanning the entire parameter space. The individual terms $\langle\Psi_0(\theta_0)|P|\Psi_0(\theta_0)\rangle$ with $P \in \{Z_0, Z_1, Z_1 Z_0, X_1 X_0, Y_1 Y_0\}$ at a list of angles $\theta_0 \in [0, 2\pi)$ are computed by preparing $|\Psi_0(\theta_0)\rangle$ using the circuit shown in Fig. 3a in

the main text and adding appropriate post-rotations (I , $-X/2$ or $Y/2$) for polarizations along different axes before measurements. Considering these estimates would be affected by stochastic fluctuations due to finite samplings, we maintain a fixed sample size of 60000 and repeat 5 times for estimating the mean values and standard deviations of each $\langle \Psi_0(\theta_0) | P | \Psi_0(\theta_0) \rangle$ at a given θ_0 . The obtained results are shown in Supplementary Fig. 6.



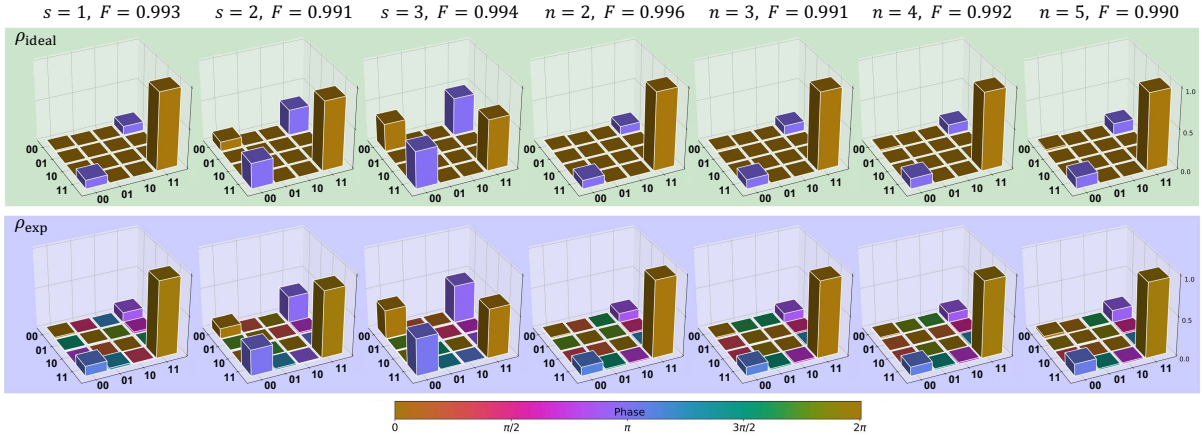
Supplementary Figure 6: Measured expectation values $\langle \Psi_0(\theta_0) | P | \Psi_0(\theta_0) \rangle$ of Pauli operators with respect to the ground state $|\Psi_0(\theta_0)\rangle$ for VQE calculations. The theoretical values are shown as solid lines, while the experimental results are shown in open circles. Error bars are smaller than the markers.

With the expansion for \hat{H}_0 (42), $E(\theta_0)$ can be computed using Eq. (54) with EM to find the optimal angle θ_0^{opt} corresponding to the position of the minimum of $E(\theta_0)$. The results are summarized in Supplementary Table 5. It is seen that for all systems we studied, the error-mitigated energies E_0^{EM} (54) are closer to the exact values than the raw energies E_0^{raw} (52). The accuracy of E_0^{EM} is on the order of the chemical accuracy (ca. 1 milli-Hartree). We also characterize the obtained ground states by quantum state tomography [21, 23] (QST). The ideal and measured density matrices are compared in Supplementary Fig. 7. The similarity between the ideal (ρ_{ideal}) and experimental (ρ_{exp}) density matrices is quantified by the state fidelity $F(\rho_{\text{ideal}}, \rho_{\text{exp}}) = \text{tr}(\sqrt{\sqrt{\rho_{\text{ideal}}} \rho_{\text{exp}} \sqrt{\rho_{\text{ideal}}}})$ [21]. For all cases, the values of F are greater than 0.990. With the determined ground states, we can evaluate the expectation values

$\langle \Psi_0 | \hat{V}^\dagger \hat{V} | \Psi_0 \rangle$ for later VQR calculations. As shown in Supplementary Table 5, similar to the energies, the error-mitigated results for $\langle \Psi_0 | \hat{V}^\dagger \hat{V} | \Psi_0 \rangle$ are significantly better than the raw results. This demonstrates the effectiveness of EM via symmetry projection also for properties other than energies.

Supplementary Table 5: VQE results for the ground states of H_2 at different bond distances $R = sR_e$ ($s = 1, 2, 3$) and polyacenes with different number of rings ($n = 2, 3, 4, 5$). θ_0^* : theoretical angle, θ_0^{opt} : VQE optimized angle, F : fidelity of the VQE ground state, E_0^* : theoretical ground-state energy, E_0^{raw} : raw energy (52), E_0^{EM} : error-mitigated energy (54).

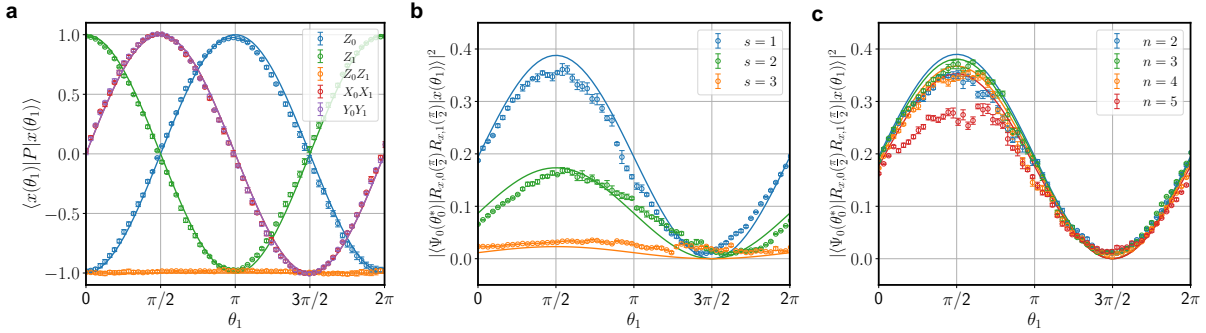
	H_2			polyacenes			
	$s = 1$	$s = 2$	$s = 3$	$n = 2$	$n = 3$	$n = 4$	$n = 5$
θ_0^*	6.0570	5.5714	5.0176	6.0610	6.0421	6.0146	5.9843
θ_0^{opt}	6.0502	5.5481	4.9902	6.0494	6.0337	6.0034	5.9704
F	0.993	0.991	0.994	0.996	0.991	0.992	0.990
E_0^*	-1.85099	-1.35779	-1.17850	-0.81072	-0.71600	-0.65279	-0.60709
E_0^{raw}	-1.83785	-1.34957	-1.17368	-0.80822	-0.71202	-0.64977	-0.60421
E_0^{EM}	-1.84563	-1.35669	-1.17625	-0.80924	-0.71431	-0.65172	-0.60591
$\langle \Psi_0 \hat{V}^\dagger \hat{V} \Psi_0 \rangle^*$	1.34575	1.46295	0.41024	3.25560	3.47443	3.73180	3.98554
$\langle \Psi_0 \hat{V}^\dagger \hat{V} \Psi_0 \rangle^{\text{raw}}$	1.37122	1.53765	0.64011	3.31827	3.66090	3.82275	4.13154
$\langle \Psi_0 \hat{V}^\dagger \hat{V} \Psi_0 \rangle^{\text{EM}}$	1.34519	1.43912	0.40241	3.27984	3.59898	3.75911	4.07832



Supplementary Figure 7: Ideal density matrices ρ_{ideal} (upper row) and experimental density matrices ρ_{exp} (lower row) determined by QST for the ground states of H_2 at $R = sR_e$ ($s = 1, 2, 3$) and polyacenes with different number of rings ($n = 2, 3, 4, 5$).

3.5 VQR experiments

The VQR calculations start with constructing the cost function $L(\theta_1)$ (14) for each interested frequency ω . To construct $\langle x|\hat{A}^\dagger(\omega)\hat{A}(\omega)|x\rangle$ in the cost function $L(\theta_1)$, we first measured the individual terms $\langle x(\theta_1)|P|x(\theta_1)\rangle$ with $P \in \{Z_0, Z_1, Z_1Z_0, X_1X_0, Y_1Y_0\}$ at a list of angles $\theta_1 \in [0, 2\pi)$. To compute the cross term (49), the quantity $|\langle 0|U_0^\dagger(\theta_0^{\text{opt}})R_{x,0}(\frac{\pi}{2})R_{x,1}(\frac{\pi}{2})U_1(\theta_1)|0\rangle|^2$ are measured using the circuit shown in Fig. 3c in the main text at the same list of θ_1 , with θ_0^{opt} obtained in the previous VQE experiments (see Supplementary Table 5). The experimental results are depicted in Supplementary Fig. 8. The errors of $|\langle 0|U_0^\dagger(\theta_0^{\text{opt}})R_{x,0}(\frac{\pi}{2})R_{x,1}(\frac{\pi}{2})U_1(\theta_1)|0\rangle|^2$ are larger than those for $\langle x(\theta_1)|P|x(\theta_1)\rangle$, due to the doubling of the number of two-qubit gates and the longer circuit length.



Supplementary Figure 8: Experimental results for quantities in the construction of VQR cost function $L(\theta_1)$ (14) for H_2 at different bond distances $R = sR_e$ ($s = 1, 2, 3$) and polyacenes with different number of rings ($n = 2, 3, 4, 5$). a, Measured expectation values $\langle x(\theta_1)|P|x(\theta_1)\rangle$ of Pauli operators with respect to the response state $|x(\theta_1)\rangle$. The theoretical values are shown as solid lines, while the experimental results are shown in open circles. Error bars are smaller than the markers. b,c, Measured $|\langle \Psi_0(\theta_0^{\text{opt}})|R_{x,0}(\frac{\pi}{2})R_{x,1}(\frac{\pi}{2})U_1(\theta_1)|0\rangle|^2$ with θ_0^{opt} in Supplementary Table 5.

The experimentally determined $\langle \Psi_0|\hat{V}^\dagger\hat{V}|\Psi_0\rangle\langle x|\hat{A}(\omega)\hat{A}(\omega)|x\rangle$ (green), $\langle \Psi_0|\hat{V}^\dagger\hat{A}(\omega)|x\rangle|^2$ (blue), and cost function $L(\theta_1)$ (black) are shown in Supplementary Fig. 9 for H_2 at different bond lengths $R = sR_e$ ($s = 1, 2, 3$), and Supplementary Fig. 10 for polyacenes with different number of rings ($n = 2, 3, 4, 5$). The position of the red vertical dashed line shows the optimized

angle θ_1^{opt} from a local quadratic fitting (red line) around the minimum for $L(\theta_1)$. The theoretical angle (black vertical line) is always $\theta_1^* = \frac{\pi}{2}$ as discussed after Eq. (41). It is seen that in certain cases such as H_2 at $R = R_e$ with $\omega = 0.6$, θ_1^{opt} deviates from θ_1^* . We find that this happens when ω is close to the triplet excitation energy ω_T , where the blue and green curves are very close to each other such that the resulting cost functions (14) as the difference between these two curves are very sensitive to experimental errors due to noises. The triplet excitation energies ω_T (in a.u.) are 0.605, 0.113, 0.011, 0.153, 0.118, 0.093, and 0.075 for H_2 at different bond lengths $R = sR_e$ ($s = 1, 2, 3$) and polyacenes with different number of rings ($n = 2, 3, 4, 5$), respectively. Therefore, we can observe similar deviations around ω_T in other cases in Supplementary Figs. 9 and 10, except for the later two systems (tetracene and pentacene), where ω_T does not lie in the energy window we are interested in, and hence do not affect the optimization, see Supplementary Figs. 10c and 10d.

Finally, with the optimized θ_1^{opt} at each frequency point ω , we can compute $\chi(\omega)$ from Eq. (18) by preparing $|x(\theta_1^{\text{opt}})\rangle$ and computing $\langle x|\hat{A}^\dagger(\omega)|x\rangle$ and $\langle x|\hat{A}^\dagger(\omega)\hat{A}(\omega)|x\rangle$ using the error mitigation technique shown in Eq. (56). The results are given in Figs. 3 and 4 in the main text for H_2 and polyacenes, respectively.

3.6 Additional results from quantum chemistry calculations

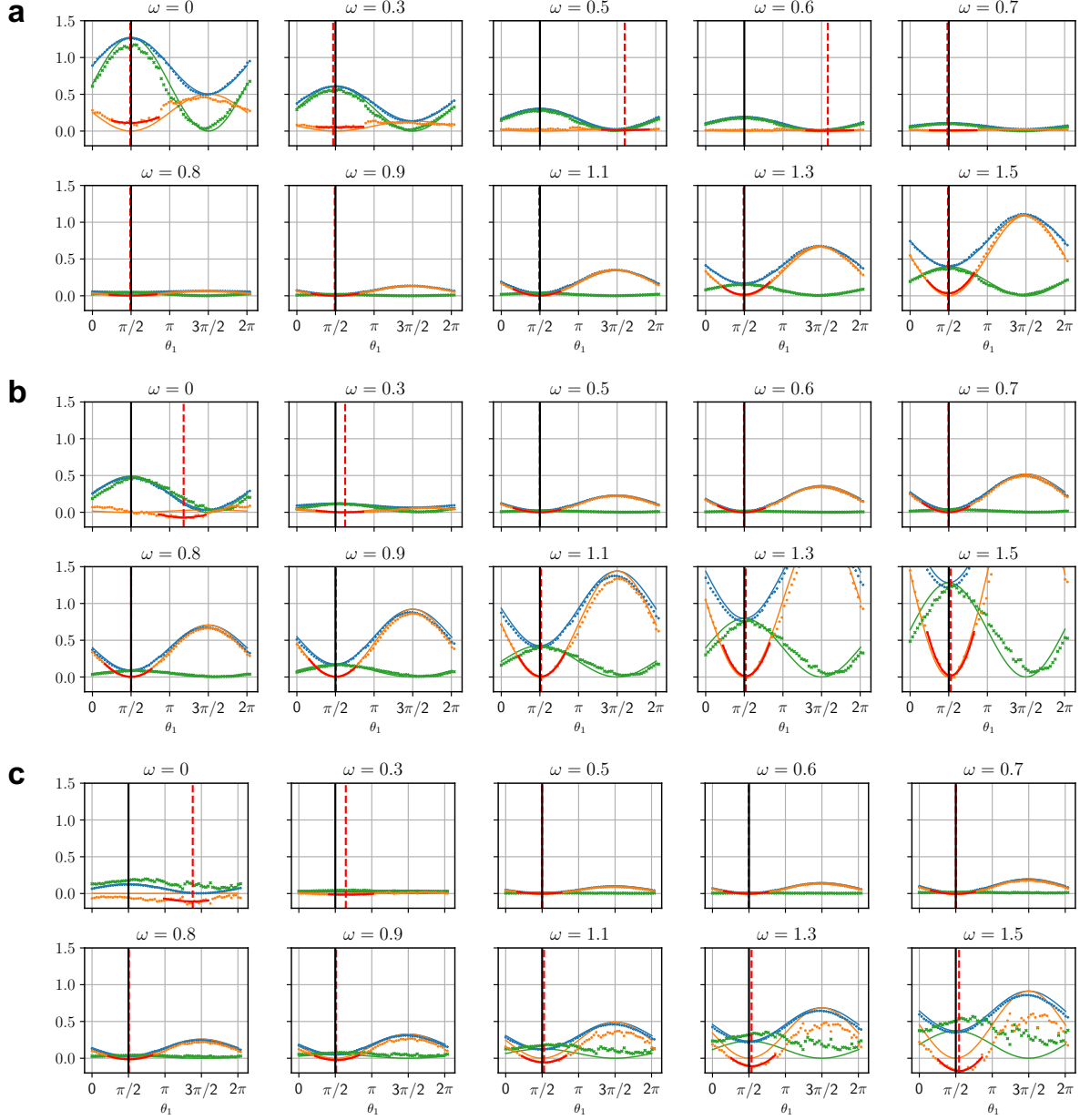
3.6.1 Dipole polarizabilities of H_2 from FCI, HF, and DFT

In Supplementary Fig. 11, we compare $\chi(\omega)$ computed using standard quantum chemistry methods including FCI, HF, and DFT with two representative exchange-correlation functionals (LDA and B3LYP) for H_2 at $R = sR_e$ ($s = 1, 2, 3$), using a locally modified version of the PySCF package [29]. It is seen that at the equilibrium HF and DFT give similar results, which are close to the FCI reference, and the spin-restricted and spin-unrestricted results coincide with each other for a given method, as symmetry breaking does not happen in the spin-unrestricted

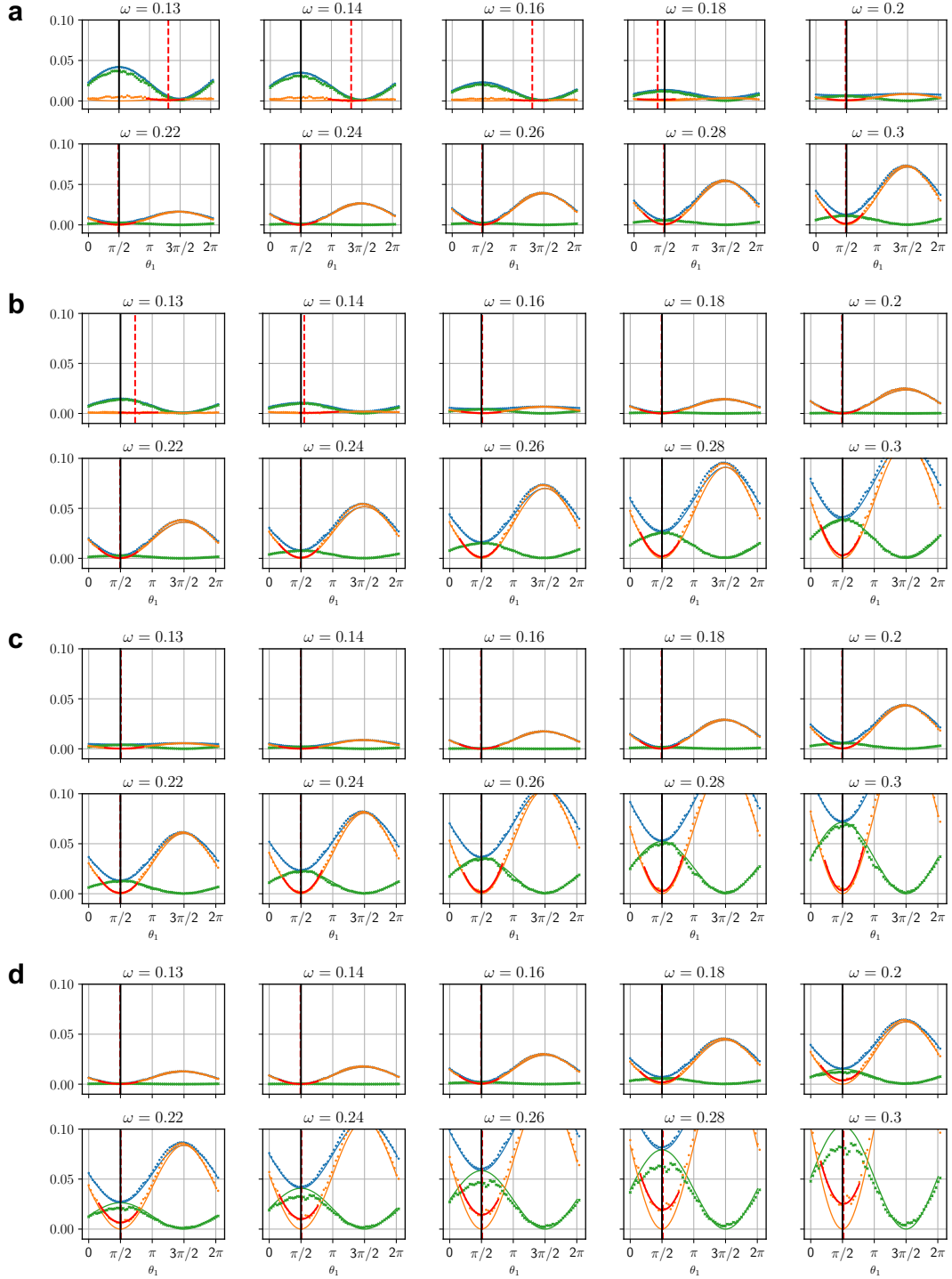
methods. However, at the stretched geometries ($s = 2$ and $s = 3$), where the electron correlation becomes much stronger than that at the equilibrium, both HF and DFT in either spin-restricted or spin-unrestricted fail even qualitatively.

3.6.2 Estimation of dynamic correlation by perturbation theory for polyacenes

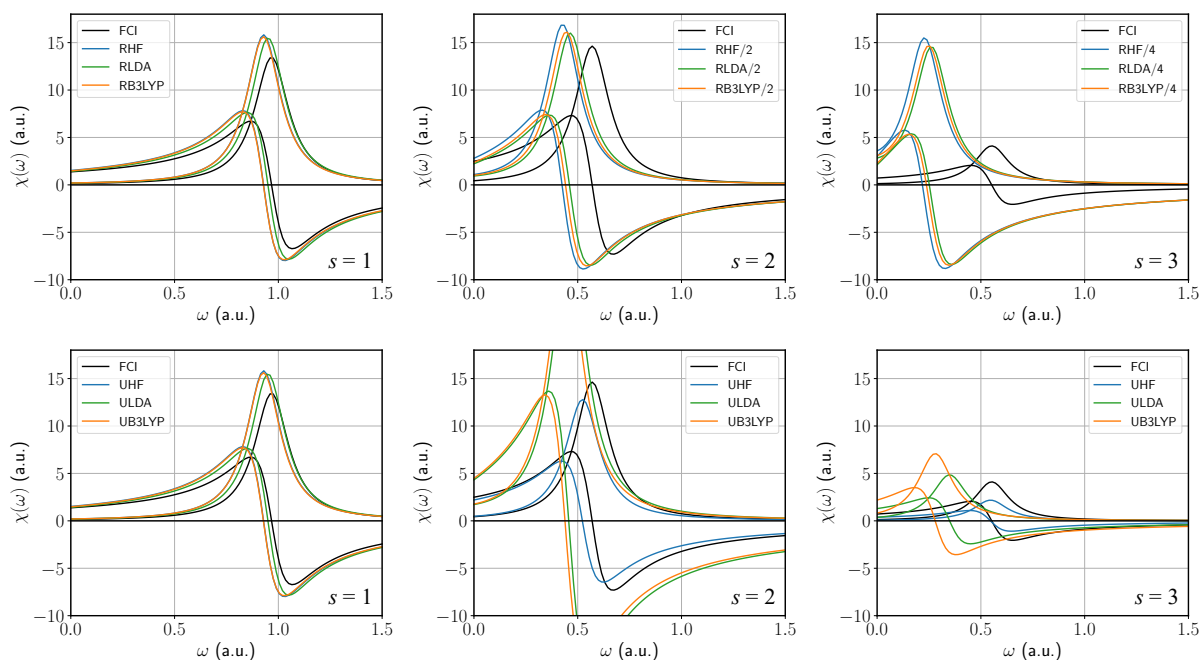
Since we adopted the active space approximation for polyacenes, the interaction between the active electrons and the frozen electrons are only treated at the mean-field level. The neglected dynamic correlation can affect the accuracy of the computed spectra. To estimate the magnitude of such effects, we compute the first excited state using the N -electron valence state perturbation theory [30] (NEVPT2) based on a complete active space configuration interaction (CASCI) reference with the RHF orbitals. The lowering of CASCI excitation energies are found to be -1.96 eV, -1.95 eV, -1.91 eV, and -1.85 eV for naphthalene ($n = 2$), anthracene ($n = 3$), tetracene ($n = 4$), and pentacene ($n = 5$), respectively. Thus, as a rough estimation of the effects of dynamic correlation on the computed spectra within the active space, we shift all the spectra by a constant -1.9 eV. The obtained results are in good agreement with the experimental spectra, see Fig. 4 in the main text. The remaining discrepancy is mainly due to the lack of the treatment of nuclear degrees of freedom, which contribute to the vibrational structures of the experimental spectra. The simulation of vibrationally resolved electronic spectra will be a subject of future study.



Supplementary Figure 9: Experimental $\langle \Psi_0 | \hat{V}^\dagger \hat{V} | \Psi_0 \rangle \langle x | \hat{A}(\omega) \hat{A}(\omega) | x \rangle$ (blue dots), $\langle \Psi_0 | \hat{V}^\dagger \hat{A}(\omega) | x \rangle^2$ (green dots), and cost function $L(\theta_1)$ (orange dots) at ten representative frequencies ω (in a.u.) for H_2 at $R = sR_e$ (a,b,c, for $s = 1, 2, 3$), with the theoretical curves shown in solid lines. The red solid line represents the fitted quadratic curve around the minimum for determining the optimal angle θ_1^{opt} (red vertical dashed line). The theoretical angle $\theta_1^* = \pi/2$ is represented by the black vertical line.



Supplementary Figure 10: Experimental $\langle \Psi_0 | \hat{V}^\dagger \hat{V} | \Psi_0 \rangle \langle x | \hat{A}(\omega) \hat{A}(\omega) | x \rangle$ (blue dots), $\langle \Psi_0 | \hat{V}^\dagger \hat{A}(\omega) | x \rangle^2$ (green dots), and cost function $L(\theta_1)$ (orange dots) at ten representative frequencies ω (in a.u.) for polyacenes with different number of rings (a,b,c,d for $n = 2, 3, 4, 5$). For other explanations, see Supplementary Fig. 9.



Supplementary Figure 11: Comparison of $\chi(\omega)$ computed using standard quantum chemistry methods including FCI, HF, and DFT with two representative exchange-correlation functionals (LDA and B3LYP) for H_2 at $R = sR_e$ ($s = 1, 2, 3$). Upper panel: spin-restricted (R) methods, Lower panel: spin-unrestricted (U) methods. Note that for $s = 2$ and $s = 3$, the results obtained with spin restricted methods are scaled by a factor of 1/2 and 1/4, respectively, in order to fit into the figure.

4 Four-qubit simulations for CO

4.1 Fermion-to-qubit mapping and wavefunction ansatz

The carbon K-edge and oxygen K-edge absorption spectra of CO are simulated with a four-electron-in-three-orbital active space model including σ_{1s_O} , σ_{1s_C} , and π_x^* orbitals obtained from RHF calculations with the STO-3G basis at the equilibrium bond length $R_e = 1.128323 \text{ \AA}$ [25]. To simplify the later simulations, we replace the active space Hamiltonian \hat{H}_0 (7) by a simplified one, in which only the molecular integrals $[p|h|p]$ and $[pp|qq]$ are kept,

$$\hat{H}_0 = \sum_p [p|h|p] a_p^\dagger a_p + \sum_{pq} \frac{1}{2} [pp|qq] a_p^\dagger a_q^\dagger a_q a_p, \quad (57)$$

where the constant E_{NN} is removed for simplicity, since it does not affect the energy difference. This is a very good approximation due to the localized nature of the core orbitals, σ_{1s_O} and σ_{1s_C} . The computed excitation energies from this approximate Hamiltonian are $\omega_C = 290.74 \text{ eV}$ and $\omega_O = 547.55 \text{ eV}$ for the singlet excited states dominated by $\sigma_{1s_C} \rightarrow \pi^*$ and $\sigma_{1s_O} \rightarrow \pi^*$, respectively, in close agreement with the values from the original active space Hamiltonian, $\omega_C = 290.94 \text{ eV}$ and $\omega_O = 547.36 \text{ eV}$. The Hartree-Fock (HF) state $|\Psi_{\text{HF}}\rangle = |\sigma_{1s_O} \sigma_{1s_C} \bar{\sigma}_{1s_O} \bar{\sigma}_{1s_C}\rangle$ is the ground state $|\Psi_0\rangle$ of the Hamiltonian (57). Within the four-electron-in-three-orbital active space model, any singlet state with Π_x symmetry can be *exactly* parameterized by

$$|x(\theta, \phi)\rangle = \cos \frac{\theta}{2} |^1\Psi_{\sigma_{1s_O} \rightarrow \pi_x^*}\rangle + \sin \frac{\theta}{2} e^{i\phi} |^1\Psi_{\sigma_{1s_C} \rightarrow \pi_x^*}\rangle, \quad (58)$$

where the singlet excited states $|^1\Psi_{\sigma_{1s_O} \rightarrow \pi_x^*}\rangle$ and $|^1\Psi_{\sigma_{1s_C} \rightarrow \pi_x^*}\rangle$ are

$$\begin{aligned} |^1\Psi_{\sigma_{1s_O} \rightarrow \pi_x^*}\rangle &= \frac{1}{\sqrt{2}} (|\pi_x^* \sigma_{1s_C} \bar{\sigma}_{1s_O} \bar{\sigma}_{1s_C}\rangle + |\sigma_{1s_O} \sigma_{1s_C} \bar{\pi}_x^* \bar{\sigma}_{1s_C}\rangle), \\ |^1\Psi_{\sigma_{1s_C} \rightarrow \pi_x^*}\rangle &= \frac{1}{\sqrt{2}} (|\sigma_{1s_O} \pi_x^* \bar{\sigma}_{1s_O} \bar{\sigma}_{1s_C}\rangle + |\sigma_{1s_O} \sigma_{1s_C} \bar{\sigma}_{1s_O} \bar{\pi}_x^*\rangle). \end{aligned} \quad (59)$$

We chose the following ordering of orbitals, such that the parity mapping [5] with the Z_2

reduction [4] for $N_e = 4$ and $N_e^\alpha = 2$ leads to

$$\begin{aligned} |n_0 n_1 n_2 n_3 n_4 n_5\rangle &= |n_{\sigma_{1sO}} n_{\pi_x^*} n_{\sigma_{1sC}} n_{\bar{\sigma}_{1sO}} n_{\bar{\pi}_x^*} n_{\bar{\sigma}_{1sC}}\rangle \\ \rightarrow |n_0(n_0 + n_1 \bmod 2) n_3(n_3 + n_4 \bmod 2)\rangle &= |q_0 q_1 q_2 q_3\rangle. \end{aligned} \quad (60)$$

As a result, the Hartree-Fock reference and the singlet excited states become

$$|\Psi_0\rangle = |1111\rangle = U_0|0000\rangle, \quad U_0 = X_0 X_1 X_2 X_3, \quad (61)$$

$$|^1\Psi_{\sigma_{1sO} \rightarrow \pi_x^*}\rangle = \frac{1}{\sqrt{2}}(|0111\rangle + |1101\rangle), \quad (62)$$

$$|^1\Psi_{\sigma_{1sC} \rightarrow \pi_x^*}\rangle = \frac{1}{\sqrt{2}}(|1011\rangle + |1110\rangle). \quad (63)$$

The circuit in Fig. 5b for Eq. (58) can be found by first preparing $|01\rangle \cos \frac{\theta}{2} + |10\rangle \sin \frac{\theta}{2} e^{i\phi}$ for the first two qubits, and then applying two entangling gates to create singlets,

$$\begin{aligned} |x(\theta, \phi)\rangle &= U_{1,3} U_{0,2} \left(|0111\rangle \cos \frac{\theta}{2} + |1011\rangle \sin \frac{\theta}{2} e^{i\phi} \right) \\ &= \frac{\cos \frac{\theta}{2}}{\sqrt{2}}(|0111\rangle + |1101\rangle) + \frac{\sin \frac{\theta}{2} e^{i\phi}}{\sqrt{2}}(|1011\rangle + |1110\rangle), \end{aligned} \quad (64)$$

where $U_{i,j}$ ($i < j$) is the entangling gate between Q_i and Q_j given by

$$U_{i,j} = \begin{bmatrix} 1 & 0 & 0 & 0 \\ 0 & \frac{1}{\sqrt{2}} & -\frac{1}{\sqrt{2}} & 0 \\ 0 & \frac{1}{\sqrt{2}} & \frac{1}{\sqrt{2}} & 0 \\ 0 & 0 & 0 & 1 \end{bmatrix} = R_{z,j}(\frac{\pi}{2}) \sqrt{i\text{SWAP}}_{i,j} R_{z,j}(-\frac{\pi}{2}). \quad (65)$$

4.2 Details of VQR algorithm

With the mapping (60), the active space Hamiltonian (57) can be written as

$$\hat{H} = \sum_{k=0}^{15} h_k P_k, \quad P_k \in \{I, Z\}^{\otimes 4}, \quad (66)$$

where the coefficients h_k are listed in Supplementary Table 6. Consequently, $\hat{A}^\dagger(\omega) \hat{A}(\omega)$ can be written as

$$\hat{A}^\dagger(\omega) \hat{A}(\omega) = \sum_{k=0}^{15} b_k(\omega) P_k, \quad P_k \in \{I, Z\}^{\otimes 4}. \quad (67)$$

with the coefficients $b_k(\omega)$ can be computed from h_k .

Supplementary Table 6: Coefficients of Pauli operators (66) in \hat{H}_0 (57) for CO.

h_{IIII}	h_{IIIZ}	h_{IIZZ}	h_{IIZI}	h_{IZII}	h_{ZZII}	h_{ZIII}	h_{IZIZ}
-40.020060	6.444399	0.495229	11.498733	6.444399	0.495229	11.498733	0.877337
h_{ZZIZ}	h_{ZIIZ}	h_{IZZZ}	h_{ZZZZ}	h_{ZIZZ}	h_{IZZI}	h_{ZZZI}	h_{ZIZI}
0.187578	0.117327	0.187578	0.148295	0.160872	0.117327	0.160872	1.186150

Here, the perturbation operator $\hat{V} = \hat{x}$ is the dipole moment operator in the x direction,

$$\hat{V} = x_O(X_0 + X_2) + x_C(X_1 + X_3), \quad x_O = -0.039321, \quad x_C = 0.079275. \quad (68)$$

By restricting the bra state to the Hartree-Fock state and the ket state in the space of the singlet excited state manifold (58), an effective operator for $\hat{V}^\dagger \hat{A}(\omega)$ can be found as

$$\begin{aligned} (\hat{V}^\dagger \hat{A}(\omega))_{\text{eff}} &= c_0(\omega)X_0 + c_1(\omega)X_1, \\ c_0(\omega) &= 2x_O[\omega_O - (\omega + i\gamma)], \\ c_1(\omega) &= 2x_C[\omega_C - (\omega + i\gamma)]. \end{aligned} \quad (69)$$

With Eq. (69), the cross term $|\langle \Psi_0 | \hat{V}^\dagger \hat{A}(\omega) | x \rangle|^2$ can be derived as

$$\begin{aligned} |\langle \Psi_0 | \hat{V}^\dagger \hat{A}(\omega) | x \rangle|^2 &= |c_0(\omega)|^2 |\langle \Psi_0 | X_0 | x \rangle|^2 + |c_1(\omega)|^2 |\langle \Psi_0 | X_1 | x \rangle|^2 \\ &\quad + 2\text{Re}(\bar{c}_0(\omega)c_1(\omega))\text{Re}(\langle x | X_0 | \Psi_0 \rangle \langle \Psi_0 | X_1 | x \rangle) \\ &\quad - 2\text{Im}(\bar{c}_0(\omega)c_1(\omega))\text{Im}(\langle x | X_0 | \Psi_0 \rangle \langle \Psi_0 | X_1 | x \rangle). \end{aligned} \quad (70)$$

The two diagonal pairs $|\langle 0 | U_0^\dagger X_k U_1 | 0 \rangle|^2$ ($k \in \{0, 1\}$) are simple to compute, because $|\Psi_0\rangle = |1111\rangle$ is a product state. Once the response state $|x(\theta, \phi)\rangle$ (64) is prepared, the probabilities P_{0111} and P_{1011} give the values for the diagonal pairs. Thus, the diagonal pairs can be computed at the same time as computing $\langle x | \hat{A}^\dagger(\omega) \hat{A}(\omega) | x \rangle$. For the off-diagonal pairs, the real part $\text{Re}(\langle x | X_0 | \Psi_0 \rangle \langle \Psi_0 | X_1 | x \rangle)$ can be computed using Eq. (33), similar to the case for H_2 . Based on Eq. (35), the imaginary part $\text{Im}(\langle 0 | U_1^\dagger X_0 U_0 | 0 \rangle \langle 0 | U_0^\dagger X_1 U_1 | 0 \rangle)$ can be computed by further noting $\langle 1111 | X_0 e^{-i\frac{\pi}{4} X_0 X_1} = \langle 1111 | X_0 e^{-i\frac{\pi}{8} (X_0 X_1 + Y_0 Y_1)} = \langle 1111 | X_0 \sqrt{i\text{SWAP}}_{0,1}$, such that

$$\text{Im}(\langle 0 | U_1^\dagger X_0 U_0 | 0 \rangle \langle 0 | U_0^\dagger X_1 U_1 | 0 \rangle) = -|\langle 0 | U_0^\dagger X_0 \sqrt{i\text{SWAP}}_{0,1} U_1 | 0 \rangle|^2 + \frac{1}{2} \left(|\langle 0 | U_0^\dagger X_0 U_1 | 0 \rangle|^2 + |\langle 0 | U_0^\dagger X_1 U_1 | 0 \rangle|^2 \right), \quad (71)$$

where the first term can be computed by preparing $\sqrt{i\text{SWAP}}_{0,1}U_1|0\rangle$ and measuring the probability P_{0111} . All the necessary components for computing the cross term $|\langle\Psi_0|\hat{V}^\dagger\hat{A}(\omega)|x\rangle|^2$ (70) are summarized in Supplementary Table 7, and the necessary quantum circuits are shown in Fig. 5b in the main text.

Supplementary Table 7: Components of $|\langle\Psi_0|\hat{V}^\dagger\hat{A}(\omega)|x\rangle|^2$ (70) in the VQR calculations for CO.

term	coefficient
$ \langle\Psi_0 X_0 x\rangle ^2$	$ c_0(\omega) ^2 - \text{Re}(\bar{c}_0(\omega)c_1(\omega)) - \text{Im}(\bar{c}_0(\omega)c_1(\omega))$
$ \langle\Psi_0 X_1 x\rangle ^2$	$ c_1(\omega) ^2 - \text{Re}(\bar{c}_0(\omega)c_1(\omega)) - \text{Im}(\bar{c}_0(\omega)c_1(\omega))$
$ \langle\Psi_0 R_{x,0}(\frac{\pi}{2})R_{x,1}(\frac{\pi}{2}) x\rangle ^2$	$4\text{Re}(\bar{c}_0(\omega)c_1(\omega))$
$ \langle\Psi_0 X_0\sqrt{i\text{SWAP}}_{0,1} x\rangle ^2$	$-2\text{Im}(\bar{c}_0(\omega)c_1(\omega))$

4.3 Error mitigation via spin symmetry projection

To improve the accuracy of computing $\langle x|\hat{A}^\dagger(\omega)\hat{A}(\omega)|x\rangle$ and $\langle x|\hat{A}^\dagger(\omega)|x\rangle$, the error mitigation (EM) strategy via symmetry projection can be used with the symmetry projector for the singlet excited state manifold (58),

$$\begin{aligned}
\mathcal{P}_S &= \mathcal{P}_S^O + \mathcal{P}_S^C, \\
\mathcal{P}_S^O &= \frac{1}{2}(|0111\rangle + |1101\rangle)(\langle 0111| + \langle 1101|) \\
&= \frac{1}{16}(I - Z_0Z_2 + X_0X_2 + Y_0Y_2)(I - Z_1)(I - Z_3), \\
\mathcal{P}_S^C &= \frac{1}{2}(|1011\rangle + |1110\rangle)(\langle 1011| + \langle 1110|) \\
&= \frac{1}{16}(I - Z_1Z_3 + X_1X_3 + Y_1Y_3)(I - Z_0)(I - Z_2).
\end{aligned} \tag{72}$$

The detailed expressions in terms of Pauli operators can be found in Supplementary Table 8. Similar to the discussion for Eq. (56), we can replace the expectation value $\langle x|P_k|x\rangle$ for P_k in $\hat{A}^\dagger(\omega)$ or $\hat{A}^\dagger(\omega)\hat{A}(\omega)$ by the error-mitigated one $\frac{\langle x|P_k\mathcal{P}_S|x\rangle}{\langle x|\mathcal{P}_S|x\rangle}$. The correspondences have been summarized in Supplementary Table 9. Apart from the measurements in the computational

basis, it is seen that this EM strategy requires $4 + 4 = 8$ groups of additional measurements for estimating terms containing XX , XY , YX , or YY for Q_0 - Q_2 or Q_1 - Q_3 .

Supplementary Table 8: Expressions for the projectors \mathcal{P}_S^O , \mathcal{P}_S^C and \mathcal{P}_S (72) in terms of Pauli operators. Operators in the same parentheses are grouped to be measured simultaneously.

projector \mathcal{P}	expression for $16\mathcal{P}$
\mathcal{P}_S^O	$(IIII - ZZZZ - IIIZ - IZII + ZZZI + ZIZZ + IZIZ - ZIZI) + (XIXI - XIXZ - XZXI + XZZX) + (YIYI - YIYZ - YZYI + YZYZ)$
\mathcal{P}_S^C	$(IIII - ZZZZ - IIZI - ZIII + ZZIZ + IZZZ + ZIZI - IZIZ) + (IXIX - ZXIX - IXZX + ZXZX) + (IYIY - ZYIY - IYZY + ZYZY)$
\mathcal{P}_S	$(2IIII - 2ZZZZ - IIIZ - IIZI - IZII - ZIII + ZZZI + ZZIZ + ZIZZ + IZZZ) + (IXIX - ZXIX - IXZX + ZXZX) + (XIXI - XIXZ - XZXI + XZZX) + (IYIY - ZYIY - IYZY + ZYZY) + (YIYI - YIYZ - YZYI + YZYZ)$

4.4 VQR experiments

To study the X-ray absorption spectra of CO, we chose 118 frequency points (ω in eV) that cover the region of interest from 230 eV to 610 eV [python code: `np.hstack((np.linspace(230, 340, 56), np.linspace(345, 495, 21), np.linspace(500, 610, 41)))`]. A broadening factor of $\gamma = 0.5$ a.u. was used. In this work, to optimize the cost function $L(\theta, \phi)$, we scan the entire parameter space, $\theta \in [0, \pi)$ and $\phi \in [0, 2\pi)$. To this end, its landscape is constructed on a two-dimensional grid (θ_i, ϕ_j) [python code: `theta=np.linspace(0.0, 3.2, 33), phi=np.linspace(0.0, 6.3, 64)`]. After balancing the effects of finite samplings, time overheads, and accuracy, each term in the cost function $L(\theta_i, \phi_j)$ is derived from the average of measurements with a fixed sample size 30000. The experimental results for $\langle \Psi_0 | \hat{V}^\dagger \hat{V} | \Psi_0 \rangle \langle x(\theta, \phi) | \hat{A}^\dagger(\omega) \hat{A}(\omega) | x(\theta, \phi) \rangle$ (with EM), $|\langle \Psi_0 | \hat{V}^\dagger \hat{A}(\omega) | x(\theta, \phi) \rangle|^2$, and $L(\theta, \phi)$ are shown in Supplementary Figs. 12, 13, and 14, respectively. The landscape of $L(\theta, \phi)$ at a given frequency ω is constructed by cubic spline interpolations and smoothing, which is used

to determine the location of the minimum and the optimized angles $(\theta^{\text{opt}}, \phi^{\text{opt}})$.

Since $\hat{A}^\dagger(\omega)\hat{A}(\omega)$ (67) is diagonal, θ is the most crucial angle for computing spectra. With Eq. (64), the theoretical value for $\langle x|\hat{A}^\dagger(\omega)\hat{A}(\omega)|x\rangle$ with the ideal angle θ^* can be found as

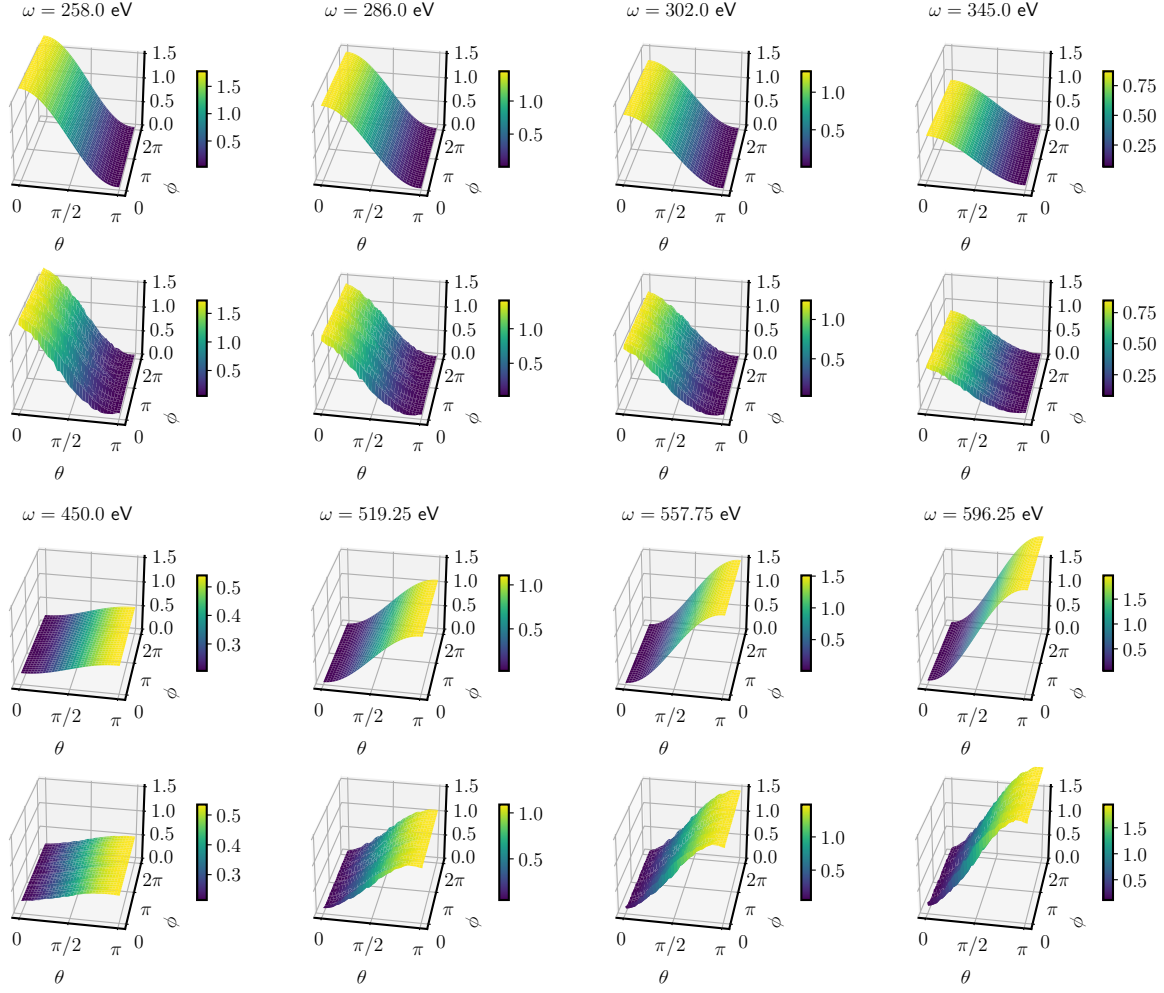
$$\begin{aligned}\langle x|\hat{A}^\dagger(\omega)\hat{A}(\omega)|x\rangle^* &= (\omega - \omega_O)^2 p_S^O + (\omega - \omega_C)^2 p_S^C + \gamma^2, \\ p_S^O &= \cos^2(\theta^*/2), \quad p_S^C = \sin^2(\theta^*/2),\end{aligned}\tag{73}$$

where p_S^O and p_S^C represent the populations of $|^1\Psi_{\sigma_{1s_O} \rightarrow \pi_x^*}\rangle$ and $|^1\Psi_{\sigma_{1s_C} \rightarrow \pi_x^*}\rangle$ in the response state, respectively. In Supplementary Fig. 15a, we compare the optimized angle θ^{opt} corresponding to the minimum of $L(\theta, \phi)$ as a function of ω with the ideal one θ^* in terms of the populations of singlets. It is seen that they agree well for ω around ω_C , whereas the deviation becomes larger for ω around ω_O . From Supplementary Fig. 14, it is seen the landscape of $L(\theta, \phi)$ is flatter around 519 eV, which makes it more susceptible to the errors of the two computed terms, $\langle \Psi_0|\hat{V}^\dagger\hat{V}|\Psi_0\rangle\langle x|\hat{A}^\dagger(\omega)\hat{A}(\omega)|x\rangle$ and $|\langle \Psi_0|\hat{V}^\dagger\hat{A}(\omega)|x\rangle|^2$. As a result, the optimized θ^{opt} exhibits a larger deviation from the ideal value in this frequency region.

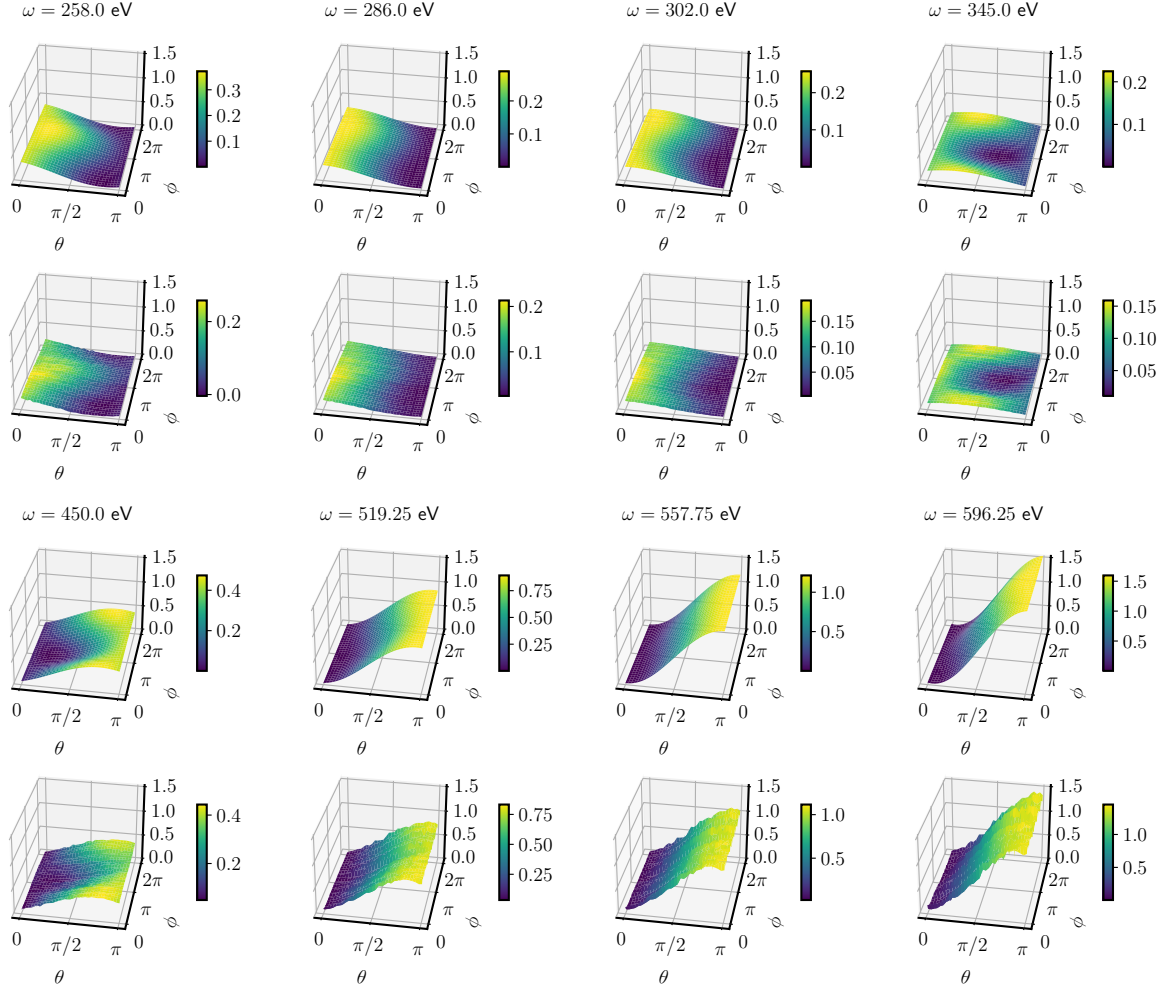
With the optimized angles $(\theta^{\text{opt}}, \phi^{\text{opt}})$, the X-ray absorption spectra can be computed by measuring $\langle x(\theta^{\text{opt}}, \phi^{\text{opt}})|\hat{A}^\dagger(\omega)\hat{A}(\omega)|x(\theta^{\text{opt}}, \phi^{\text{opt}})\rangle$ for each ω , see Eq. (20). In Supplementary Fig. 15b, we compare the raw experimental results and the error-mitigated results for $\langle x|\hat{A}^\dagger(\omega)\hat{A}(\omega)|x\rangle$ at the optimized $(\theta^{\text{opt}}, \phi^{\text{opt}})$ (labelled by raw and EM) and the ideal (θ^*, ϕ^*) (labelled by raw* and EM*), against the theoretical curve (73). It is clear that using EM significantly improves the accuracy of $\langle x|\hat{A}^\dagger(\omega)\hat{A}(\omega)|x\rangle$, and hence the computed spectra shown in Fig. 5c in the main text. The deviations of the EM results computed with the ideal angles from the theoretical curve is solely due to the errors in computing $\langle x|\hat{A}^\dagger(\omega)\hat{A}(\omega)|x\rangle$ with QPU.

Supplementary Table 9: Error mitigation strategy using \mathcal{P}_S for estimating the expectation values of $\langle x|P_k|x\rangle$ by $\frac{\langle x|P_k\mathcal{P}_S|x\rangle}{\langle x|\mathcal{P}_S|x\rangle}$. Operators in the same parentheses are grouped to be measured simultaneously.

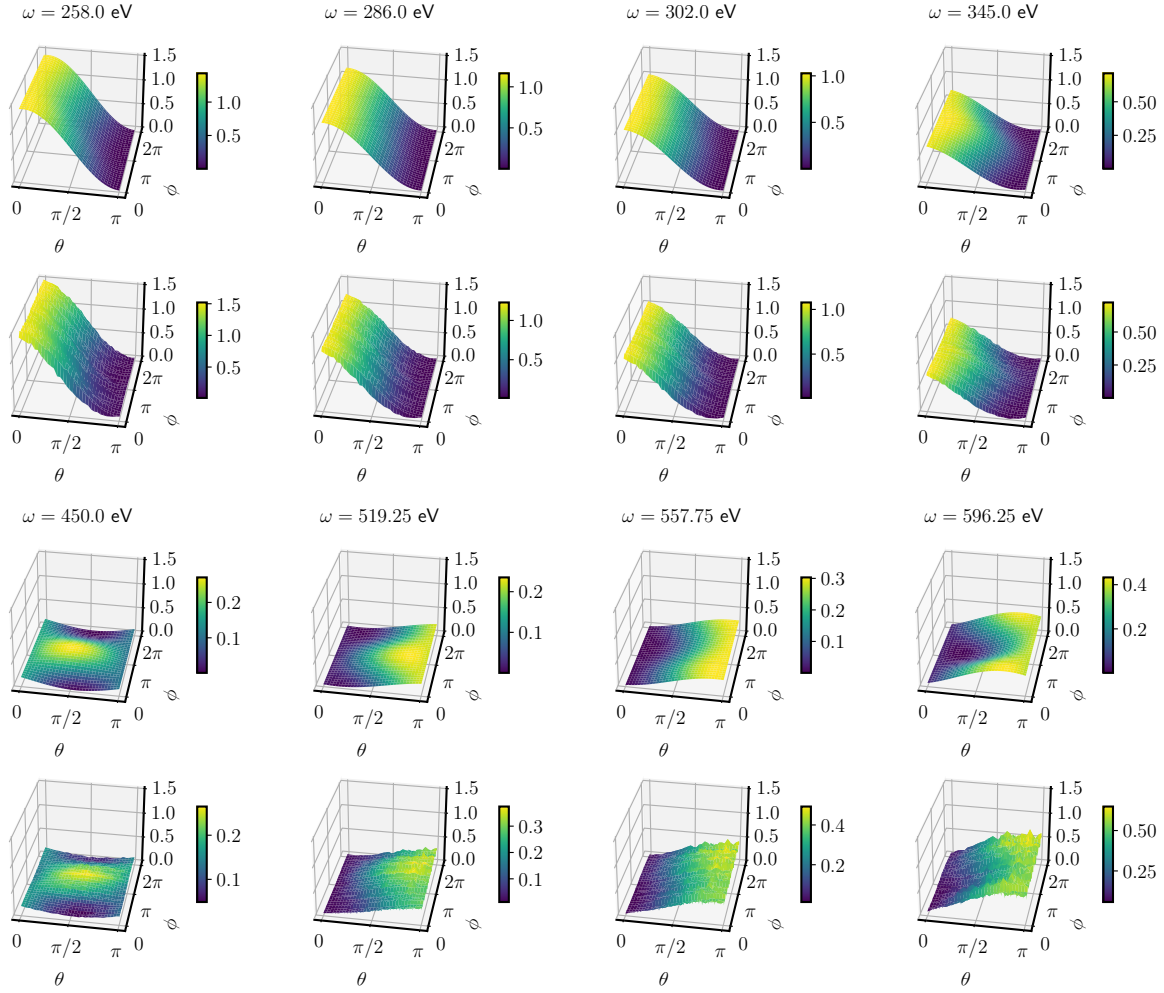
P_k	$16P_k\mathcal{P}^S$
$IIII$	$(2IIII - 2ZZZZ - IIIZ - IIZI - IZII - ZIII + ZZZI + ZZIZ + ZIZZ + IZZZ) + (IXIX - ZXIX - IXZX + ZXZX) + (XIXI - XIXZ - XZXI + XZXZ) + (IYIY - ZYIY - IYZY + ZYZY) + (YIYI - YIYZ - YZYI + YZYZ)$
$ZZZZ$	$(2ZZZZ - 2IIII + IIIZ + IIZI + IZII + ZIII - ZZZI - ZZIZ - ZIZZ - IZZZ) - (IXIX - ZXIX - IXZX + ZXZX) - (XIXI - XIXZ - XZXI + XZXZ) - (IYIY - ZYIY - IYZY + ZYZY) - (YIYI - YIYZ - YZYI + YZYZ)$
$ZIZI$	$(2ZIZI - 2IZIZ + IIIZ - IIZI + IZII - ZIII - ZZZI + ZZIZ - ZIZZ + IZZZ) + (IXIX - ZXIX - IXZX + ZXZX) - (XIXI - XIXZ - XZXI + XZXZ) + (IYIY - ZYIY - IYZY + ZYZY) - (YIYI - YIYZ - YZYI + YZYZ)$
$IZIZ$	$(-2ZIZI + 2IZIZ - IIIZ + IIZI - IZII + ZIII + ZZZI - ZZIZ + ZIZZ - IZZZ) - (IXIX - ZXIX - IXZX + ZXZX) + (XIXI - XIXZ - XZXI + XZXZ) - (IYIY - ZYIY - IYZY + ZYZY) + (YIYI - YIYZ - YZYI + YZYZ)$
$IIIZ$	$(2IIIZ - 2ZZZI - IIZZ - ZIIZ + ZZII + IZZI - IIII + ZIZI - IZIZ + ZZZZ) - (XIXI - XIXZ - XZXI + XZXZ) - (YIYI - YIYZ - YZYI + YZYZ) + i[(IXIY - ZXIY - IXZY + ZXZY) - (IYIX - ZYIX - IYZX + ZYXZ)]$
$ZZZI$	$(2ZZZI - 2IIIZ + IIZZ + ZIIZ - ZZII - IZZI + IIII - ZIZI + IZIZ - ZZZZ) + (XIXI - XIXZ - XZXI + XZXZ) + (YIYI - YIYZ - YZYI + YZYZ) - i[(IXIY - ZXIY - IXZY + ZXZY) - (IYIX - ZYIX - IYZX + ZYXZ)]$
$IIZI$	$(2IIZI - 2ZZIZ - IIZZ + ZIIZ + ZZII - IZZI - IIII - ZIZI + IZIZ + ZZZZ) - (IXIX - ZXIX - IXZX + ZXZX) - (IYIY - ZYIY - IYZY + ZYZY) + i[(XIIY - XIYZ - XZYI + XZYZ) - (YIXI - YIXZ - YZXI + YZXZ)]$
$ZZIZ$	$(2ZZIZ - 2IIZI + IIZZ - ZIIZ - ZZII + IZZI + IIII + ZIZI - IZIZ - ZZZZ) + (IXIX - ZXIX - IXZX + ZXZX) + (IYIY - ZYIY - IYZY + ZYZY) - i[(XIIY - XIYZ - XZYI + XZYZ) - (YIXI - YIXZ - YZXI + YZXZ)]$
$IZII$	$(2IZII - 2ZIZZ + IIZZ + ZIIZ - ZZII - IZZI - IIII + ZIZI - IZIZ + ZZZZ) - (XIXI - XIXZ - XZXI + XZXZ) - (YIYI - YIYZ - YZYI + YZYZ) - i[(IXIY - ZXIY - IXZY + ZXZY) - (IYIX - ZYIX - IYZX + ZYXZ)]$
$ZIZZ$	$(2ZIZZ - 2IZII - IIZZ - ZIIZ + ZZII + IZZI + IIII - ZIZI + IZIZ - ZZZZ) + (XIXI - XIXZ - XZXI + XZXZ) + (YIYI - YIYZ - YZYI + YZYZ) + i[(IXIY - ZXIY - IXZY + ZXZY) - (IYIX - ZYIX - IYZX + ZYXZ)]$
$ZIII$	$(2ZIII - 2ZZZZ + IIZZ - ZIIZ + ZZII + IZZI - IIII - ZIZI + IZIZ + ZZZZ) - (IXIX - ZXIX - IXZX + ZXZX) - (IYIY - ZYIY - IYZY + ZYZY) - i[(XIIY - XIYZ - XZYI + XZYZ) - (YIXI - YIXZ - YZXI + YZXZ)]$
$IZZZ$	$(2IZZZ - 2ZIII - IIZZ + ZIIZ + ZZII - IZZI + IIII + ZIZI - IZIZ - ZZZZ) + (IXIX - ZXIX - IXZX + ZXZX) + (IYIY - ZYIY - IYZY + ZYZY) + i[(XIIY - XIYZ - XZYI + XZYZ) - (YIXI - YIXZ - YZXI + YZXZ)]$
$ZZII$	$(2ZZII - 2IIZZ + IIIZ + IIZI - IZII - ZIII - ZZZI - ZZIZ + ZIZZ + IZZZ) + i[(IXIY - ZXIY - IXZY + ZXZY) + (XIIY - XIYZ - XZYI + XZYZ) - (IYIX - ZYIX - IYZX + ZYXZ) - (YIXI - YIXZ - YZXI + YZXZ)]$
$IIZZ$	$(2IIZZ - 2ZZII - IIIZ - IIZI + IZII + ZIII + ZZZI + ZZIZ - ZIZZ - IZZZ) - i[(IXIY - ZXIY - IXZY + ZXZY) + (XIIY - XIYZ - XZYI + XZYZ) - (IYIX - ZYIX - IYZX + ZYXZ) - (YIXI - YIXZ - YZXI + YZXZ)]$
$IZZI$	$(2IZZI - 2ZIIZ + IIIZ - IIZI - IZII + ZIII - ZZZI + ZZIZ + ZIZZ - IZZZ) + i[(IXIY - ZXIY - IXZY + ZXZY) - (XIIY - XIYZ - XZYI + XZYZ) - (IYIX - ZYIX - IYZX + ZYXZ) + (YIXI - YIXZ - YZXI + YZXZ)]$
$ZIIZ$	$(2ZIIZ - 2ZZZI - IIIZ + IIZI + IZII - ZIII + ZZZI - ZZIZ - ZIZZ + IZZZ) - i[(IXIY - ZXIY - IXZY + ZXZY) - (XIIY - XIYZ - XZYI + XZYZ) - (IYIX - ZYIX - IYZX + ZYXZ) + (YIXI - YIXZ - YZXI + YZXZ)]$



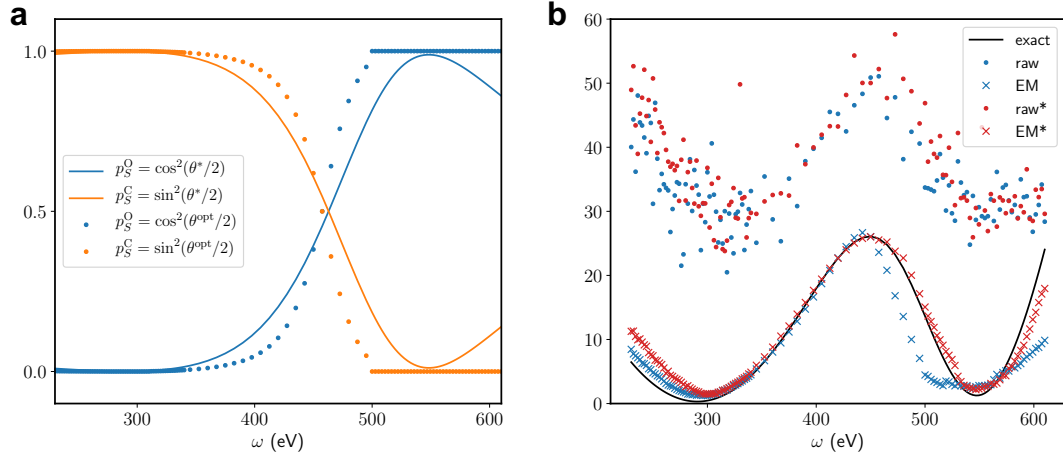
Supplementary Figure 12: Ideal (upper row) and experimental (lower row) results for the landscapes of $\langle \Psi_0 | \hat{V}^\dagger \hat{V} | \Psi_0 \rangle \langle x(\theta, \phi) | \hat{A}^\dagger(\omega) \hat{A}(\omega) | x(\theta, \phi) \rangle$ at eight representative frequencies ω .



Supplementary Figure 13: Ideal (upper row) and experimental (lower row) results for the landscapes of $|\langle \Psi_0 | \hat{V}^\dagger \hat{A}(\omega) | x(\theta, \phi) \rangle|^2$ at eight representative frequencies ω .



Supplementary Figure 14: Ideal (upper row) and experimental (lower row) results for the landscapes of the cost function $L(\theta, \phi)$ at eight representative frequencies ω .



Supplementary Figure 15: Experimental results for the optimized angles θ and the computed $\langle x | \hat{A}^\dagger(\omega) \hat{A}(\omega) | x \rangle$ for $\chi(\omega)$ in the VQR calculations for CO. a, The optimized θ^{opt} compared against the ideal θ^* at each frequency. b, The raw experimental results and the error-mitigated results for $\langle x | \hat{A}^\dagger(\omega) \hat{A}(\omega) | x \rangle$ at the optimized θ^{opt} (labelled by raw and EM) and the ideal θ^* (labelled by raw* and EM*), compared against the theoretical curve (the black line) $\langle x | \hat{A}^\dagger(\omega) \hat{A}(\omega) | x \rangle^*$ (73).

References

- [1] Norman, P., Ruud, K. & Saue, T. *Principles and practices of molecular properties: Theory, modeling, and simulations* (John Wiley & Sons, 2018).
- [2] Helgaker, T., Jørgensen, P. & Olsen, J. *Molecular electronic-structure theory* (John Wiley & Sons, 2014).
- [3] Jordan, P. & Wigner, E. About the pauli exclusion principle. *Z. Phys.* **47**, 631 (1928).
- [4] Bravyi, S. & Kitaev, A. Y. Fermionic quantum computation. *Ann. Phys.* **298**, 210–226 (2002).
- [5] Seeley, J. T., Richard, M. J. & Love, P. J. The bravyi-kitaev transformation for quantum computation of electronic structure. *J. Chem. Phys.* **137**, 224109 (2012).
- [6] Peruzzo, A. *et al.* A variational eigenvalue solver on a photonic quantum processor. *Nat. Commun.* **5**, 4213 (2014).
- [7] McClean, J. R., Romero, J., Babbush, R. & Aspuru-Guzik, A. The theory of variational hybrid quantum-classical algorithms. *New J. Phys.* **18**, 023023 (2016).
- [8] Cai, X., Fang, W.-H., Fan, H. & Li, Z. Quantum computation of molecular response properties. *Phys. Rev. Res.* **2**, 033324 (2020).
- [9] Xu, X. *et al.* Variational algorithms for linear algebra. *arXiv preprint arXiv:1909.03898* (2019).
- [10] Bravo-Prieto, C. *et al.* Variational quantum linear solver. *arXiv preprint arXiv:1909.05820* (2019).

- [11] Motta, M. *et al.* Low rank representations for quantum simulation of electronic structure. *npj Quantum Inf.* **7**, 1–7 (2021).
- [12] Huggins, W. J. *et al.* Efficient and noise resilient measurements for quantum chemistry on near-term quantum computers. *npj Quantum Inf.* **7**, 1–9 (2021).
- [13] Boyd, R. W. *Nonlinear optics* (Elsevier, 2003).
- [14] Somma, R., Ortiz, G., Gubernatis, J. E., Knill, E. & Laflamme, R. Simulating physical phenomena by quantum networks. *Phys. Rev. A* **65**, 042323 (2002).
- [15] Ibe, Y. *et al.* Calculating transition amplitudes by variational quantum deflation. *arXiv preprint arXiv:2002.11724* (2020).
- [16] Song, C. *et al.* Generation of multicomponent atomic schrödinger cat states of up to 20 qubits. *Science* **365**, 574–577 (2019).
- [17] Motzoi, F., Gambetta, J. M., Rebentrost, P. & Wilhelm, F. K. Simple pulses for elimination of leakage in weakly nonlinear qubits. *Phys. Rev. Lett.* **103**, 110501 (2009).
- [18] Zheng, Y. *et al.* Solving systems of linear equations with a superconducting quantum processor. *Phys. Rev. Lett.* **118**, 210504 (2017).
- [19] Song, C. *et al.* 10-qubit entanglement and parallel logic operations with a superconducting circuit. *Phys. Rev. Lett.* **119**, 180511 (2017).
- [20] Huang, K. *et al.* Quantum generative adversarial networks with multiple superconducting qubits. *npj Quantum Inf.* **7**, 1–5 (2021).
- [21] Chuang, I. L. & Nielsen, M. A. Prescription for experimental determination of the dynamics of a quantum black box. *J. Mod. Opt.* **44**, 2455 (1997).

- [22] Guo, Q. *et al.* Dephasing-insensitive quantum information storage and processing with superconducting qubits. *Phys. Rev. Lett.* **121**, 130501 (2018).
- [23] Nielsen, M. A. & Chuang, I. L. *Quantum computation and quantum information* (Cambridge University Press, 2010).
- [24] Trotzky, S. *et al.* Time-resolved observation and control of superexchange interactions with ultracold atoms in optical lattices. *Science* **319**, 295–299 (2008).
- [25] Huber, K. P. & Herzberg, G. *Molecular Spectra and Molecular Structure IV. Constants of Diatomic Molecules* (Van Nostrand Reinhold, New York, 1979).
- [26] Becke, A. D. Becke’s three parameter hybrid method using the lyp correlation functional. *J. Chem. Phys* **98**, 5648–5652 (1993).
- [27] Stephens, P. J., Devlin, F. J., Chabalowski, C. F. & Frisch, M. J. Ab initio calculation of vibrational absorption and circular dichroism spectra using density functional force fields. *J. Phys. Chem.* **98**, 11623–11627 (1994).
- [28] Bravyi, S., Gambetta, J. M., Mezzacapo, A. & Temme, K. Tapering off qubits to simulate fermionic hamiltonians. *arXiv preprint arXiv:1701.08213* (2017).
- [29] Sun, Q. *et al.* Pyscf: the python-based simulations of chemistry framework. *Wiley Interdiscip. Rev. Comput. Mol. Sci.* **8**, e1340 (2018).
- [30] Angeli, C., Cimiraglia, R., Evangelisti, S., Leininger, T. & Malrieu, J.-P. Introduction of n-electron valence states for multireference perturbation theory. *J. Chem. Phys.* **114**, 10252–10264 (2001).